REPORT DOCUMENTATION PAGE

Form Approved
OMB No. 0704-0188

Public reporting burden for this collection of information is estimated to average 1 hour per response, including the time for reviewing instructions, searching existing data sources, gathering and maintaining the data needed, and completing and reviewing this collection of information. Send comments regarding this burden estimate or any other aspect of this collection of information, including suggestions for reducing this burden to Department of Defense, Washington Headquarters Services, Directorate for Information Operations and Reports (0704-0188), 1215 Jefferson Davis Highway, Suite 1204, Arlington, VA 22202-4302. Respondents should be aware that notwithstanding any other provision of law, no person shall be subject to any penalty for failing to comply with a collection of information if it does not display a currently valid OMB control number. **PLEASE DO NOT RETURN YOUR FORM TO THE ABOVE ADDRESS.**

1. REPORT DATE *(DD-MM-YYYY)* 02-25-2011	**2. REPORT TYPE** Final Report	**3. DATES COVERED** *(From - To)* Dec 2007-Nov 2010

4. TITLE AND SUBTITLE
YIP-08 Hypervelocity Boundary Layer Studies for Axisymmetric Engine Flowpaths

5a. CONTRACT NUMBER

5b. GRANT NUMBER
FA9550-08-1-0172

5c. PROGRAM ELEMENT NUMBER

6. AUTHOR(S)
Austin, Joanna, M.

5d. PROJECT NUMBER

5e. TASK NUMBER

5f. WORK UNIT NUMBER

7. PERFORMING ORGANIZATION NAME(S) AND ADDRESS(ES)

University of Illinois
1901 South First St, Ste A
South Research Park
Champaign IL 61820-7406

8. PERFORMING ORGANIZATION REPORT NUMBER

9. SPONSORING / MONITORING AGENCY NAME(S) AND ADDRESS(ES)
Air Force Office of
Scientific Research
875 N Randolph St Rm 3122
Arlington VA 22203
Joyce A. Burch

Program Manager:
Dr John Schmisseur

10. SPONSOR/MONITOR'S ACRONYM(S)
AFOSR

11. SPONSOR/MONITOR'S REPORT NUMBER(S)
AFRL-OSR-VA-TR-2012-0249

12. DISTRIBUTION / AVAILABILITY STATEMENT
Approved for Public Release; Distribution is Unlimited

13. SUPPLEMENTARY NOTES

14. ABSTRACT

An experimental and analytical study of boundary layer response to concave surface curvature in a high-stagnation enthalpy, hypersonic flow is reported. Data for models with cubic, quadratic and blended concave surface curvature were compared with two baseline models: a flat plate and a linear compression ramp. Diagnostic capabilities for surface heat transfer and two-dimensional surface pressure measurements were developed. For all models, concave surface curvature was shown to produce significant destabilization of the boundary layer and increase in the heat flux over flat plate laminar and tripped boundary layer values. We have demonstrated that the laminar heat flux has a functional form that is very similar to the surface equation, and therefore that a reasonable estimate for the increase in heat transfer may be made from the surface geometry at the conditions of these experiments. Imposed vortex structures exhibited significant differences in the response to surface curvature. Spanwise pressure gradients were measured in the presence of the vortex structures, but not in their absence. The vortex structures were observed to interact with the pressure gradient. The distance to vortex breakdown was quantified and found to depend strongly on the surface curvature.

15. SUBJECT TERMS
Hypervelocity boundary layers, mechanical distortions, concave surface geometry

16. SECURITY CLASSIFICATION OF:			**17. LIMITATION OF ABSTRACT**	**18. NUMBER OF PAGES**	**19a. NAME OF RESPONSIBLE PERSON** Prof. Joanna Austin
a. REPORT (U)	**b. ABSTRACT** (U)	**c. THIS PAGE** (U)	(UU)	77	**19b. TELEPHONE NUMBER** *(include area code)* 217 333 3739

Final Report for Award YIP-08
Hypervelocity Boundary Layer Studies for Axisymmetric Engine Flowpaths
Award number # FA9550-08-1-0172

Joanna M. Austin and William P. Flaherty
Department of Aerospace Engineering
University of Illinois
Urbana, IL 61801

February 25, 2011

An experimental and analytical study of boundary layer response to concave surface curvature in a high-stagnation enthalpy, hypersonic flow is reported. An expansion tube impulse facility was used to generate a Mach 5.4 freestream. Data for four models with cubic, quadratic and blended concave surface curvature were compared with two baseline models: a flat plate and a linear compression ramp with the same final turning angle as one of the concave ramps. Diagnostic capabilities for surface heat transfer and two-dimensional surface pressure measurements with fast response times were developed, as well as the capability for visualization of imposed vortical structures along the models.

Baseline data over a flat plate show heat transfer levels in reasonable agreement with the expected Simeonides prediction for the laminar hypervelocity boundary layer. For a tripped boundary layer, the heat transfer levels recover to reasonable agreement with the Van Driest II correlation, however, as discussed below, pressure sensitive paint measurements were able to provide more information on boundary layer structures. Data for four models with concave surface curvature show significant destabilization of the boundary layer in all cases. The laminar heat flux over the concave surfaces was up to a factor of 20 greater than the flat plate values. The heat flux over the curved ramp was less than that measured on the linear compression ramp with the same final turning angle. We have demonstrated that for the laminar boundary layer over the compression ramps studied, the heat flux dependence on downstream distance has a functional form that is very similar to the surface equation, and therefore that a reasonable estimate for the increase in heat transfer may be made from the surface geometry at the conditions of these experiments.

Vortex structures were imposed into the flow using protuberance strips and pressure sensitive paint was used to observe significant differences in the response of these

structures to surface curvature. Spanwise pressure gradients were measured in the presence of the vortex structures, but not in their absence. The vortex structures were observed to interact with the pressure gradient and were swept towards and away from the centerline of the curved model. The distance to vortex breakdown was quantified and found to depend strongly on the surface curvature. Work is continuing past the end of this award to model the vortex dynamics observed in these experiments. We hope to use the significant differences in vortex response over the different surface geometries as a diagnostic tool for development of structure evolution models in hypervelocity boundary layers.

1 Introduction

1.1 Background

To date, hypersonic vehicle engine designs have been almost universally two-dimensional. The recent interest in axisymmetric scramjet engines is motivated by improved performance predictions from the inlet to the combustor, including higher efficiency, improved structural integrity, and reduced skin friction. Inward-turning hypersonic vehicle inlets have the theoretical potential to achieve higher efficiencies than conventional two-dimensional geometries [1, 2]. The inward-turning or axisymmetric Busemann inlet concept exploits streamline tracing during flow compression through the inlet to minimize entropy production and stagnation pressure loss and therefore maximize efficiency. An inward turning inlet naturally terminates in an elliptical cross-section. In a dual mode scramjet engine, the compressed flow then propagates though the isolator section into the combustor. An elliptical combustor geometry has reduced skin friction drag and improved structural integrity, and is therefore highly desirable. The entirely axisymmetric scramjet engine has received substantial recent interest as a design that incorporates these performance advantages. A key new aspect of these geometries is their concave surfaces. Unlike convex geometries that are relevant to the external aerodynamics of the vehicle, flows over concave geometries have received relatively little attention to date. Yet detailed design of axisymmetric engine flowpaths depends on our ability to model and predict boundary layers and other flow features over such surfaces.

In this work, we examine boundary layers flows, which are known to be significantly influenced by three-dimensional effects, at high stagnation-enthalpy, hypersonic conditions. At lower speeds, the stability and heat transfer of boundary layers developing in the presence of pressure gradients over a concave surface, with possible Goertler vortex formation, are known to depart significantly from flat-plate theory.

Numerous studies have examined compressible boundary layers over a flat plate (see, for example, reviews by Bradshaw [3]; Spina, Smits, Robinson [4]), although the general behavior is still not completely understood, particularly where no analogy with low speed turbulent flows may be made as in cases where turbulent motions respond strongly to pressure gradients or interact with shock waves [5]. An axisymmetric engine boundary layer will undoubtably encounter both strong pressure gradients and shock wave impingment making Morkovins hypothesis of limited use in predicting the vehicle performance [6].

In addition, thermochemical processes such as dissociation and vibrational excitation are known to have a significant impact on the gasdynamics in a hypersonic flow (for example, Wen and Hornung [7], Gnoffo [8], among many others). A critical question that confronts vehicle designers is the role of such thermochemical effects on transition and turbulence in the boundary layer.

Significant complexity is introduced if a realistic vehicle surface geometry is considered rather than the flat plate. Pressure gradients may act in all three dimensions simultaneously and significant regions of three-dimensional flow can occur. Experiments by Donovan [9] in a Mach 2.9 flow, showed the absolute wall shear stress increased by about 125% and the skin friction by about 77% over a concave wall. In contrast, an adverse pressure gradient causes the wall shear stress to decrease in a subsonic flow. Fernando and Smits found that strong turbulent mixing with a thin sonic layer increases the wall stress, and the skin friction continues to increase well after the end of the concave region, and even after the pressure gradient has ended [10].

If the surface is curved, a moving fluid element is subject to an additional centrifugal instability mechanism. Stationary counter-rotating vortices known as Goertler vortices [11] are observed to form on concave walls under certain conditions, although there is considerable uncertainty in the literature as to which conditions (Smits and Dussauge [5]). The formation of these vortices influences turbulence and fluid mixing. Goertler vortices have been observed in supersonic boundary layers over concave surfaces, for example, on nozzle walls (Beckwith and Holley [12], Beckwith et al. [13]). de Luca et al. experimentally observed Goertler vortices in a Mach 7 flow and found 20-30% fluctuations in heat transfer with respect to the spanwise average [14]. Fu, Hall and Blackenby showed that the temperature adjustment layer at the edge of the boundary layer is most susceptible to Goertler instability [15]. Depending on the degree of curvature and the free stream conditions, Goertler instability may be the primary instability mechanism of the boundary layer [16].

1.2 Objectives of this Study

The main goals of this study were to:

Determine how the boundary layer heat transfer and growth rate are modified by the surface geometry. Experimental measurements of boundary layers over concave ramps (cubic, quadratic, and blended surface equations), linear compression ramp, and flat plate model surfaces were made in a high-enthalpy, hypersonic flow. Diagnostic capabilities for heat transfer and surface pressure measurements were developed to meet experimental challenges and measurement capabilities were tested using several techniques. Laminar and tripped boundary layers were studied.

Examine the response of imposed vortex structures to global mechanical distortions by surface geometry. Protuberance elements were used to impose longitudinal vortex structures into the boundary layer, and the response of these structures to the surface geometry was visualized along the models. Four different protuberance strip geometries were investigated. The heat transfer behind one of these strips was measured for the different geometries. The evolution and breakdown of the vortex structures was quantified and the generation of spanwise effects for vortices over compression ramps was investigated.

Anticipate the need for boundary layer data for input and physics-based modeling of flow over de-stabilizing surface geometries. Performance predictions for novel vehicle geometries such as the inward-turning inlet depend significant on the boundary layer model used. A validation quality database was generated with attention to free stream characterization, multi-instrument measurements and comparison to baseline models. These data have been disseminated in archival publications and at conference presentations, with additional publications in preparation.

1.3 Organization of this Report and Principal Results

The experimental capabilities developed for surface heat transfer measurements and full-field pressure measurements are described in Section 3, and validation of these gages is described in Section 6. The principal conclusions in these section are:

1. **Comparative heat transfer measurements using thermocouple and thin film gauges show good agreement.** Thermocouples and thin film gages are used extensively for surface heat transfer measurements in hypersonic impulse facilities. Coaxial thermocouples are robust, can survive challenging experimental conditions, and are typically used in higher enthalpy flows. Thin film resistance gages provide improved signal levels, but have to be individually calibrated, are less robust, and are typically used in lower enthalpy flows. As a result there are few studies directly comparing heat flux measurements from both these gage types. Both gages have been successfully used in the Hypervelocity Expansion Tube over an intermediate enthalpy range between 4.08 and 7.52 MJ/kg. Spherical and flat plate models were both tested, and the heat transfer data are consistent.

2. **Pressure sensitive paint was demonstrated to achieve adequate response times and survive the hypervelocity experimental conditions.** The response time of the paint was demonstrated to be sufficient to obtain qualitative pressure distributions and streamwise vortex visualizations over multiple model geometries in a hypersonic test environment. The vortex structure, frequency and breakdown distance could be estimated from the data. Comparisons with static pressure measurements made using pressure taps show differences of up to a factor of three, and calibration sources as well as an alternative lifetime measurement method remain to be investigated.

Six model geometries were selected for this study: a flat plate, a linear compression ramp, and four ramps with concave surface curvature. Details of the experiments are presented in Sections 7 to 11. Section 7 includes laminar and tripped boundary layer results for the baseline flat plate model. Section 8 includes laminar and tripped boundary layer results for the straight and curved compression ramps. Section 10 reviews predictive models for curved compression surfaces, and the work that was done implementing these models for the current study. Results for all models are then compared in the next two sections.

The principal conclusions for laminar boundary layer studies over these ramps are:

1. **Significant destabilization of boundary layer occurs over the compression ramps.** The laminar boundary layer heat transfer over the baseline flat plate was in good agreement with existing predictions. For the concave geometry, a factor of 20 increase in heat transfer over flat plate results was measured. The linear compression ramp had a factor of two increase in heat transfer compared to the curved compression ramp with the same final turning angle.

2. **The heat transfer over the compression ramps appear to have the same functional form as the surface geometry.** Curve fits to the heat transfer data for each model geometry showed that the increase in heat transfer could be correlated with the surface curvature. The heat transfer over the three quadratic and the cubic surfaces was fit by quadratic and cubic equations respectively, providing a simple means of initially estimating the effect of surface curvature on heat flux.

Rapid prototyping technology was used to create trip strips of different geometries. The principal conclusions for the tripped boundary layer studies are

1. **Heat transfer levels behind the protuberance strips recover to Van Dreist II levels over a flat plate.** The protuberances had dimensions on the order of the boundary layer thickness, and so produced a significant overshoot ("over-tripping") in the heat transfer. By a streamwise location 11% of the plate length, the data over the flat plate was in reasonable agreement with the Van Dreist II correlation.

2. **A factor of 20 increase in the heat transfer was measured over the concave ramps with respect to the flat plate.** With the protuberances installed the linear ramp had only a 13% increase over the curved compression ramp of the same final turning angle.

The trip elements also act as protuberances which generate vortical structures. As discussed in Section 11, visualization of the vortex response to the model surface geometry was made possible with the fast-response pressure paint. The principal conclusions are:

1. **The vortical structures displayed a strong response to surface geometry.** Over the linear ramp, the vortices were observed to sweep out away from the centerline of the model in response to a spanwise pressure gradient. Over the concave ramp, the vortices were observed to sweep in towards the centerline of the model, and then sweep out. The breakdown range of these vortices was quantified from the image intensity. The vortices were maintained over the concave surface to the end of the model, while breakdown occurred within 53 and 50 % of the plate length for the flat plate and linear compression ramp respectively.

2. **Pressure sensitive paint measurements showed a mean, spanwise flow induced by the vortices over the curved and linear ramps, but not over the flat plate.** No spanwise pressure gradient was measured for any ramp in the absence of the vortices. The striking differences displayed by the both mean flow and vortical elements, in a coupled fashion, over the different surface geometry continue to be analyzed past the end of this award.

2 Facility description

All experiments for this project were carried out in the Hypervelocity Expansion Tube (HET) in the P.I.'s lab at the University of Illinois. The HET is an expansion tube facility which operates across a range of Mach numbers from 3.0 to 7.5 and stagnation enthalpies from 4.0 to 8.0 MJ/kg [17]. The 9.14 m long facility consists of driver, driven, and accelerator sections all with a 150 mm inner diameter. The driver and driven section are separated by a metal diaphragm, while the driven and accelerator sections are separated by a thin plastic diaphragm. Test conditions can be changed simply by changing the fill pressures and gases in the three sections of the tube. Theoretically, any test gas could be used in the driven section. Air, CO2, and Argon have all been used as test gases in the HET. Accelerator gas is also varied depending on the run condition, and is typically helium or air [17].

Operation of the tube begins by filling all three sections to different pressures. The driver section is evacuated vacuum (around 200 mtorr), the driven section is evacuated to a pressure typically between 1 to 6 kPa, and the accelerator section is evacuated to a pressure of a few hundred mtorr. This process is done iteratively in order to avoid rupturing the thin secondary diaphragm (which can tolerate approximately a 20 kPa difference in pressure between sections). The pressures in the driven and the accelerator sections are varied based on what run condition is desired for that shot. Once all three sections are at the required pressure, the driver section is pressurized to around 2.5 MPa, causing the primary diaphragm to rupture. This is referenced as time zero on the x-t diagram shown in Figure 1. This high pressure ratio across the diaphragm causes a shock to propagate through the driven section, causing mass movement in the test gas. After the initial shock has passed through the test gas, the test gas is at condition two (indicated on the x-t diagram). When this initial shock reaches the secondary diaphragm it ruptures it. This results in a transmitted shock which propagates through the accelerator section (inducing mass motion in the accelerator gas, indicated as condition six in the x-t diagram), as well as an unsteady expansion fan as the reflected wave. The gas in the driven section is accelerated through this expansion fan to hypersonic velocities (indicated as condition seven on the x-t diagram). From the perspective of a model mounted in the test section of the HET, it first experiences the transmitted shock. This shock is followed by the accelerator gas, which has been put in motion by the transmitted shock. Next, over a finite time, comes the interface between the accelerator gas and the test gas. Following the contact surface will be the test gas. The time during which the model is exposed to the test gas is denoted as the "test time". Termination of the test time occurs when the tail or the reflected head of the unsteady expansion wave reaches the test section. In run conditions used in the HET it is most commonly the expansion tail which arrives in the test section first and terminates the test time, but it is theoretically possible to create a run condition which is terminated by the expansion head. Finally, the driver gas passes over the model. This portion of the shot is the most mechanically stressful to the model as the driver gas has the highest stagnation pressure. Thus, when determining the forces exerted on the model (in order to design it to be safe to mount in the tube) the burst pressure of the diaphragm should be used as the highest pressure exerted on the blunt faces of the model. A typical pitot probe trace, spanning from the arrival of the initial shock to the termination of the test gas, is shown in Figure 2, and a picture of the HET facility can be seen in Figure 3.

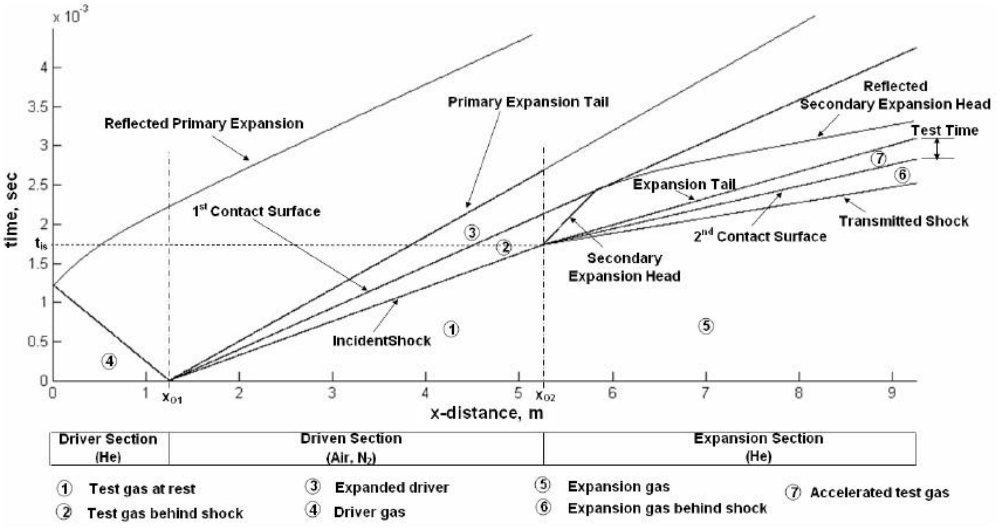
x 10^-3
time, sec
t_is
4
3.5
3
2.5
2
1.5
1
0.5
0
0
1
x_O1
2
3
4
5
x_O2
6
7
8
9
x-distance, m
Reflected Primary Expansion
Primary Expansion Tail
Reflected
Secondary Expansion Head
Test Time
1st Contact Surface
Expansion Tail
2nd Contact Surface
Transmitted Shock
Secondary
Expansion Head
IncidentShock
①
②
③
④
⑤
⑥
⑦
Driver Section
(He)
Driven Section
(Air, N2)
Expansion Section
(He)
① Test gas at rest
② Test gas behind shock
③ Expanded driver
④ Driver gas
⑤ Expansion gas
⑥ Expansion gas behind shock
⑦ Accelerated test gas

Figure 1: Sample x-t diagram for HET operation [18]

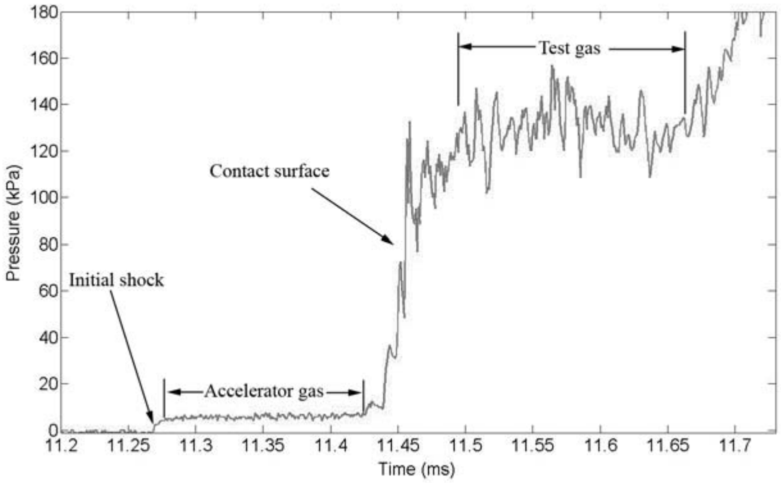

Figure 2: Sample pitot trace in the HET

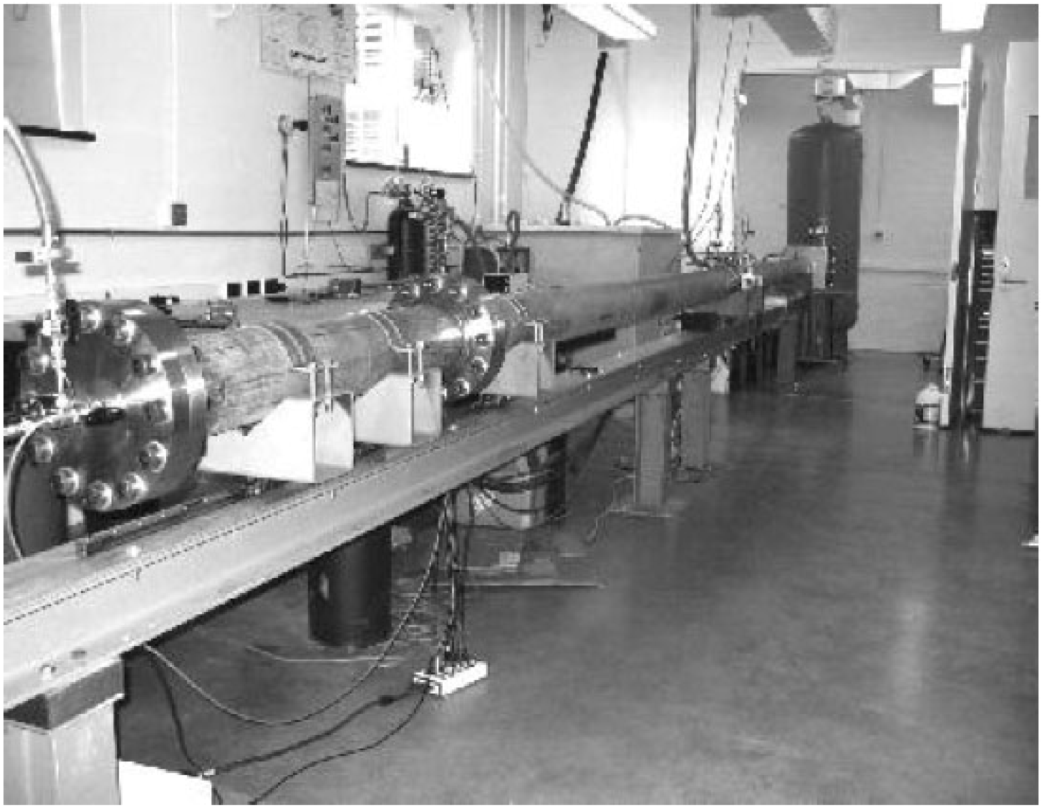

Figure 3: HET facility

3 Development and demonstration of diagnostic techniques

3.1 Previous implementation of heat transfer gages

In the course of this project both coaxial thermocouple and thin film heat transfer gages were implemented in the facility, allowing multiple options to measure heat flux [19, 20]. Thermocouple and thin film gages have been used to measure heat transfer in a number of super/hypersonic facilities since the 1950's. The work done in this project implementing them into the P.I.'s facility at the University of Illinois drew on these works to assist in overcoming experimental obstacles.

Miller [21] performed a comprehensive review of thin film gages used in the NASA Langley Continuous Flow Hypersonic Tunnel (CFHT), comparing their performance to thick-skin calorimeters. Gage durability on both glass and ceramic substrates were tested. It was found that of the four glass substrate models, only one survived longer than one test. The ceramic models fared slightly better, with one surviving six tests, and the other surviving all nine tests it was subjected to. Since these tests were conducted in a continuous-flow facility the gages were exposed to test times three orders of magnitude longer than typical impulse facility test times. The method used to apply the gages to the substrate was significantly different than the current technique which could have significant effects on gage durability. Chadwick [22] performed a detailed review of the use of thin film heat transfer gages in the CUBRC 96 inch reflected shock tunnel facility. Heat transfer data are obtained at multiple run conditions with enthalpies ranging from 1.85 to 7.44 MJ/kg and Mach numbers from 10 to 16.

Kidd presents a detailed survey of the coaxial thermocouples used at Arnold Air Force Base, as well as many other facilities [23]. Some issues associated with the coaxial gages are quantified. The two major conclusions from this study were that coaxial thermocouples can be utilized at test times much longer than semi-infinite body assumption would allow, and also that the gage length does not need to be equal to the model wall thickness. In a later study, Kidd et al. investigated the effects of extraneous voltages caused by electrical connections between the model and the gage, and found that care must be taken to minimize the effects of such contact [24].

Coaxial thermocouple gages are typically used in high stagnation enthalpy flows in the Caltech T5 reflected shock tunnel facility. Sanderson [25] originally developed a new coaxial thermocouple design in order to avoid fragility issues associated with thin film gages, and other issues with the more generally used coaxial wire thermocouples. Sanderson found that extraneous voltages produced from contact between the gage and the model were negligible with the new design. These thermocouples have been applied to other experiments in the T5 facility [26, 27, 28]. Marineau and Hornung [29] performed a numerical study of the gages designed by Sanderson. The response time and accuracy of the gages was found to be strongly dependent on the junction geometry. A simultaneous calibration procedure for multiple gages is proposed if individual calibration is desired.

Salvador et al. report on the development of coaxial thermocouple gages for use in the shock tunnel facilities at the Laboratory for Aerothermodynamics and Hypersonics in Brazil [30]. One important result from this paper is the demonstration of the dependence of gage response time on the connection properties between the two electrodes. It was found that simply by using different grit sandpaper to create the junction the response time could change by a factor of two.

While not focused on direct comparative measurements, there are a limited number of studies in which both thin film and thermocouple surface heat transfer data are available. In a recent study at the National Aerospace Laboratory in Japan, both coaxial and thin film thermocouples were used to compare the operation of the Hypersonic Wind Tunnel, the High Enthalpy Shock Tube, and the Hypersonic Shock Tube to establish guidelines for the use of the facilities [31]. The thermocouple data were found to be in good agreement with IR thermography, and the non-dimensional heat transfer agreed to within a few percent between all three facilities. Both thin film and thermocouple gages were used in two recent studies at CUBRC. The first study focused on real gas effects in both the LENS I and LENS X facilities for test gas enthalpies from 2 to 12 MJ/kg [32]. Heating rates measured by both gages were in good agreement with each other, however at high enthalpies the measured heat flux did not agree with either fully catalytic or non-catalytic wall predictions. The second study at CUBRC, conducted in the LENS I reflected shock tunnel, used the gages to investigate the role of catalytic effects on a sphere-cone model in both nitrogen and carbon dioxide. Tests were run at test gas enthalpies of 2, 6, and 8 MJ/kg. This study found good agreement between the gages, but found that all gage types measured heating levels higher than predicted assuming a non-catalytic wall, but less than that predicted assuming a fully-catalytic wall [33].

3.2 Thermocouple Development

Surface mounted thermocouples are very common sensors used for the measurement of the surface temperature histories in impulse facilities. Thermocouples operate using the Seebeck effect, which states that when two dissimilar metals are joined there is a measurable voltage difference between the two wires which changes with temperature [34]. One of the most basic and widely used thermocouple designs is two wires with different composition joined together using either a simple solder or a weld. While these types of thermocouples are extremely robust and easy to manufacture, they suffer from slow response times and the inability to be surface mounted. Due to the short test times in impulse facilities as well as the desire to get surface data, it is necessary to develop new thermocouple designs to overcome these problems. Since the early 1950's, many impulse facilities have utilized coaxial wire thermocouples. These gages are constructed out of a thin tube of one electrode material, and a solid wire of the second electrode material. The solid wire is drawn through the tubular electrode, and insulated from it by a thin lair of an electrically insulating material. The gage is then installed in a model such that the surface of the gage is parallel with the surface of the model. The top of the gage is then sanded. During this sanding process, strands of the metal from the inner electrode are brought into contact with the outer electrode, creating the thermocouple junction [24]. This sanding process is extremely important to the eventual properties of the gage (such as response time). While this design overcomes the issues of typical thermocouples, it is not without drawbacks. The junction created by sanding can result in inconsistent gage response times, and the long lengths of the gages can cause them to act as antennas, picking up ambient electrical noise. The thermocouples used in these experiments are based on the design of Sanderson [25]. These thermocouples were designed specifically to avoid the issues with the more common coaxial wire thermocouples. They are coaxial, 2.4 mm in diameter, type E (Constantan-Chromel), and mount flush with the surface of a model. The two coaxial elements are designed such that an extremely thin junction (on the order of 1 μm) is formed at the surface. An image of these two electrodes compared to a penny can be seen in Figure 4.

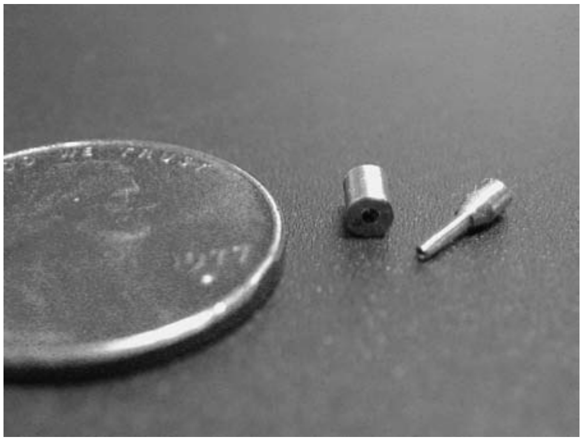

Figure 4: Thermocouple electrodes.

This type of thermocouple gage is used extensively in the T5 reflected shock tunnel at GALCIT [25, 26, 27], where the high enthalpy test conditions result in adequate signal levels and the robust design of the gages make them highly resistant to damage caused by particulates in the test gas as well as the large heat fluxes [25]. Technical drawings of the thermocouples, as well as advice on their construction, was provided by the T5 group at Caltech. Initially, it was attempted to make the thermocouples completely in house at the University of Illinois. To aid in this purpose a MicroLux variable speed bench lathe was procured. The appropriate equipment was purchased so that the small thermocouple elements could be properly mounted in the chuck. The type E thermocouple material was purchased from Omega Engineering. Initial attempts to manufacture the thermocouples resulted in multiple setbacks. The larger outer electrodes proved relatively easy to machine, but the much smaller inner electrodes proved to be extremely difficult, and very few survived the machining process. The small "stem" of the inner electrode had an outer diameter of only 0.025 inches, and it was found to be extremely difficult to make this cut on the lathe without bending the stem at the same time. During this period a series of guidelines for making the gages was developed:

1. Sharp, hand-ground tools were most effective, and it was imperative to keep a large supply of freshly sharpened tools.
2. When aligning the tool, care was taken to ensure that the cutting edge would hit the stock first, otherwise the small stock may bend away.

3. When taking cuts for the electrodes the entire cut was taken in one pass. While this may result in a non-optimal surface finish, repeat passes increase the chance of the electrode bending.

4. When using small drill bits the bit was brought as close to the stock as possible with the slide, and the hand wheel was kept loose. This helped to prevent the small bit from breaking.

5. Keep both RPM and feed rates low. The RPM was set to approximately 140 to drill and 240 to turn the thermocouple material.

6. A small amount of play was allowed for in the slides (especially the angle slide). If the slides were kept too tight the stock had a higher chance of bending during the machining process.

A small number of working thermocouples were developed during this phase of the project. These thermocouples were installed in a stagnation sphere and tested in the HET. Though the signals obtained were far too noisy to be of practical use, the signal level was good enough to confirm that the thermocouples would be usable in the HET. Due to the extremely large time commitment required to produce the thermocouples it was decided to farm the machining work out to a machine shop which specialized in producing small parts, and keep the assembly of the individual thermocouples in house. It was decided to use Pacific Precision Inc. in California as they are the same machine shop used by the Caltech T5 group, and therefore already had experience manufacturing these thermocouples. Though the cost per thermocouple was higher than producing them in house, it was still substantially lower than if the gages had been bought commercially. Once the two electrodes have been made (whether in or out of house), they must be assembled in a specific way in order to ensure gage functionality as well as the proper response time. The two electrodes must be joined together using a layer of epoxy in order both to mechanically hold them together as well as insulate the electrodes from each other at all locations other than the surface junction. Also, when joining the two electrodes together they must be pressed together with enough force to create the surface junction, but not too much force so that it causes the sharp contact point between the two electrodes to deform. This deformation can result in problems with response time and signal level. A special form was designed and machined in order to hold the two electrodes together while the epoxy dried. An illustration of an ideal junction can be seen in Figure 5.

Secondly, wires must be soldered to each individual electrode so that the signal from the junction can be fed out of the test section. This soldering process is extremely delicate, as the wires are 30 gage and the holes are of a correspondingly small diameter. Care must be taken to ensure that the solder junction is strong and that the two electrodes are not soldered together. The first method developed to assemble the thermocouples involved epoxying the two electrodes together first, waiting for the epoxy to dry, and then soldering the wires to the electrodes. This introduced one major problem to the construction process. It was necessary during the soldering process to keep the soldering iron at almost the max temperature possible. If the iron was in contact with the electrode for too long it could result in a softening of the epoxy joining the electrodes, causing the junction between the

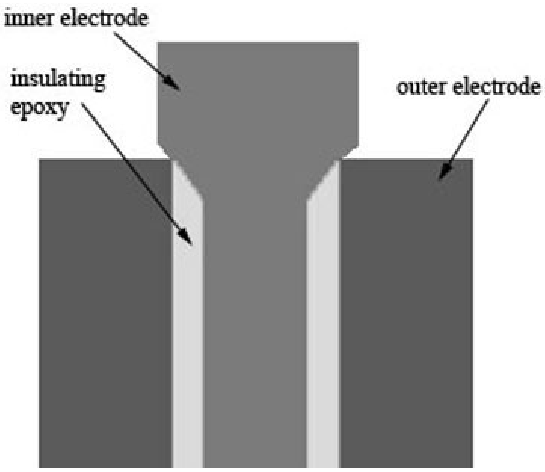

Figure 5: Sketch of thermocouple junction.

two electrodes to fail. This resulted in a broken thermocouple which must be thrown away. It was later determined that the wires could be soldered to the electrodes before they were joined using the epoxy. This eliminates the issue encountered previously and resulted in a much higher thermocouple survival rate. The form for holding the drying thermocouple had to be slightly modified to allow this new method, but this modification posed no issues. After the two electrodes are joined together and the wires are soldered to the back, a small bead of epoxy is placed on the back of the thermocouple to add support to the solder junctions. Once the epoxy bead has dried the thermocouple is ready for installation in the model. The thermocouple is inserted (wire first) through the top of the model. Next, its sides are coated with a thick layer of super glue and it is inserted into the model. A razor blade is used to align the top of the thermocouple with the top of the model. Once the super glue has dried, the protruding pin is removed using a fine tooth jewelers saw and the thermocouple is filed until it is flat with the surface of the model. Finally, 500 grit sandpaper is used to sand the junction. Multiple sandpaper grits were tested and 500 grit was found to produce the most consistent thermocouple response. Throughout the entire assembly process, it is useful to check the resistance between the two wires at every stage. A good, working thermocouple will typically have a resistance between 0.9 and 1.4 Ohms. Unfortunately there is no way to determine the response time of a thermocouple before it has been used in a test in the HET. A preliminary way to check the response time is a visual inspection of the junction after installation. The thermocouple should lie almost flat with the surface, and the junction should be highly polished. It should be difficult to to see the line between the two electrodes. The best way to determine if the gage response time is high enough is to check the gage's response to the incident shock in the HET. If the gage registers an almost discontinuous change in temperature as a result of the shock passage then it can be considered to have a high enough response time.

The signal is fed out of the test section through a 42 pin KF50 flanged feedthrough from Kurt J. Lesker. On the vacuum side the thermocouple wires are soldered to individual female D-sub connector pins. On the air side, custom cables are used to connect the feedthrough to the signal conditioners. These connectors are made of RG58 coaxial cable.

On one end the signal wire of the cable is soldered to a female D-sub pin, and care is taken to ensure that it is not connected to the grounding shield of the cable. The other end of the cable consists of a female BNC connector. The output signal is then passed to a differential amplifier circuit mounted exterior to the test section. The circuit consists of 2 stages of gain, both using an OP27 low noise op amp. This circuit also serves to eliminate the effects of any extraneous voltages generated between the thermocouple and the model wall. The circuit gain is 1000 to maximize signal amplitude. Due to the fact that all resistors have an inherent deviation from their intended resistance, the theoretical gain of the circuit will not be equal to the actual gain. As such it was necessary to measure the gain of each channel individually so that the correct gain number would be used when deconvolving the temperature signal. The gain of each channel was calculated by inputting a low amplitude sine wave signal whose frequency was similar to that of the changes in temperature during a shot. This frequency matching was important to ensure that there was no gain distortion at higher frequencies. Since the amplifier was set to have such a high gain it was necessary to measure each channel's stages individually in order to avoid saturation. It was assumed that there were no losses in the connections between the two amplifiers so that the total channel gain was recovered by multiplying the gains of the individual stages together. The circuit diagram can be seen in Figure 6a. Individual calibration of thermocouples is not necessary, since the temperature response of all common thermocouple types is well known. The NIST thermocouple reference tables were used to convert from voltage to temperature [35].

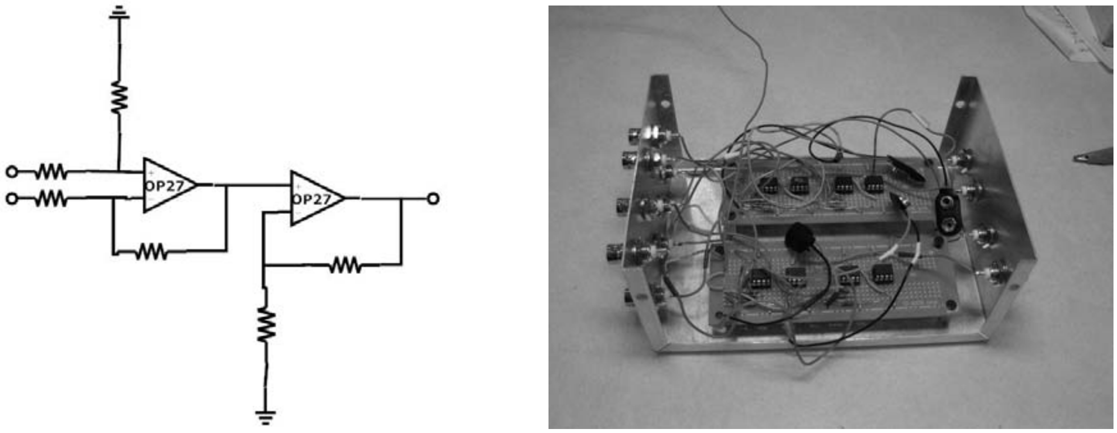

(a) Circuit diagram.

(b) Circuit box

Figure 6: Circuit diagram and circuit box for thermocouples.

3.3 Thin Film Gage Development

The thin film gages used in this study are based on the design of Adelgren [36], Chadwick [22], and Kinnear [37]. The gages operate based on the temperature-resistance relationship of platinum. A thin strip of platinum will have a given resistance at room temperature. As the temperature of the substrate the strip is mounted on changes, there will be a corresponding change in the resistance of the platinum strip. This response is linear, and can be determined through calibration. Since resistance is a difficult measurement to make during an experiment, the gage is used as one arm in a basic Wheatstone bridge circuit, thus converting from a temperature-resistance to a temperature-voltage relationship. The details of this circuitry will be given later in this section.

Gage construction begins by painting a thin strip of metallo-organic platinum paint on an insulating substrate, typically a form of glass or ceramic (for these experiments MACOR®was used). Henceforth the term "gage" will be defined as the insulating substrate with the thin strip of platinum painted on it. After the platinum is painted on the substrate, the gage is fired in a kiln. Multiple different firing profiles are reported in the literature for constructing the gages, and it was decided to determine a unique firing profile tailored to the furnace being used. The overall temperature settings were based on those used by Adelgren [36]. The piece was placed in the furnace and it was set to reach a maximum temperature of 642 Celsius at a ramp rate of 5 degrees per minute. This resulted in a run time of approximately 2 hours, at which point the kiln was turned off and the gage was allowed to cool overnight. This cooling period is extremely important as if the gage is removed prematurely it can result in thermal stresses causing micro-cracks in the strip of platinum paint, which can cause the gage to become non-functional. Next, this process is repeated with metallo-organic silver paint which is used to create electrical leads to the strip of platinum paint. They are fired using the same profile as the original platinum strip. At this point it should be possible to measure the resistance across the gage using the two silver leads. The gage should have a target resistance somewhere between 100 and 500 Ohms. If the gage resistance is too high, it can be lowered by painting and firing additional strips of platinum paint over the original gage. If this is done, it is important to also paint a slight layer of metallo-organic silver paint over the leads, as it is possible they will be baked away during the subsequent firings unless reinforced with more silver paint. Once the gage is within the target range wires are attached to the silver leads using a conductive silver epoxy. Similar to the thermocouples, this wire can then be fed through the test section and into a circuit. The circuit used with these gages is a simple Wheatstone bridge circuit coupled with a single stage amplifier. The Wheatstone bridge consists of four arms, two on a left branch, and two on a right branch. The left branch arms consist of two matched, fixed resistors. These form the reference branch of the bridge. The first arm on the right branch is the thin film gage, and the second is a trimming potentiometer. The outputs of the bridge are measured after the first arms of the left and right branches. These outputs are used as inputs to a single stage differential amplifier of similar design to those used with the thermocouples. The gain of the amplifier is set to a theoretical level of 100, but it is not necessary to measure it exactly as it is taken into account during the calibration procedure. A sketch of the circuit and the actual circuit box can be seen in Figure 7.

At the beginning of a test (when the gage is at room temperature) the trimming potentiometer is adjusted until the output of the circuit is approximately zero volts, this is known as the balanced condition. As the surface temperature(and correspondingly the resistance) of the gage changes, the bridge will be thrown out of balance and the circuit will output a voltage that is proportional to the change in resistance of the thin film gage. Since this change will be different for every gage, they must be individually calibrated. Where the sensitivity of the thermocouple gages is set solely by the type of metals used, the sensitiv-

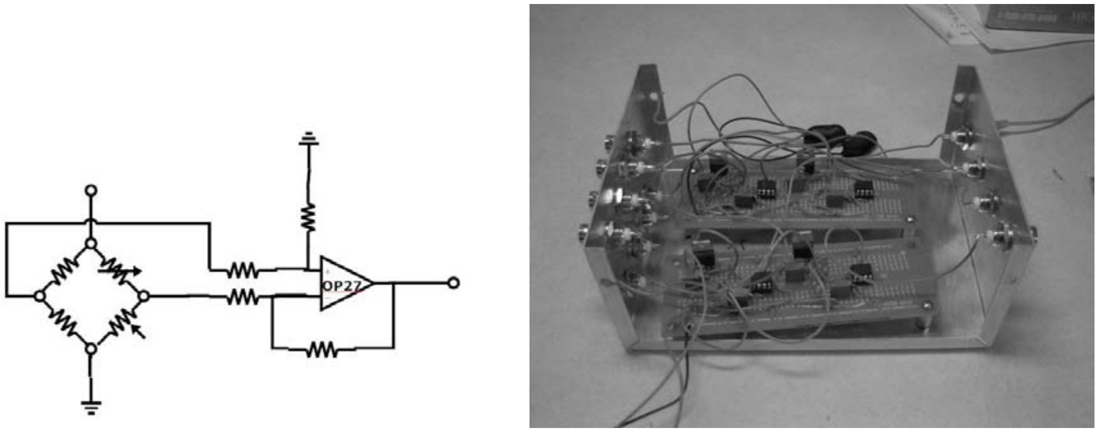

(a) Thin film circuit diagram.

(b) Thin film circuit box

Figure 7: Circuit diagram and circuit box for thinfilm gages.

ity of the thin film gages is highly dependent on gage geometry (including the size, shape, and thickness of the platinum strip). It is for this reason that the gage must be handled extremely carefully after it is constructed. Even small scratches to the surface of the gage can result in a change to the gage sensitivity. Two different methods were investigated to calibrate the gages. The first method was suggested by Adelgren in his Ph.D. thesis [36]. During this calibration procedure, a bath of a non-conducting fluid (glycerol) is brought to a known temperature (measured with a commercial thermocouple). The bath is heated using two thermal tapes and a PID temperature controller purchased from Omega Engineering. It was found that when using the PID controller that only the proportional gain control should be used. When integral and derivative control was attempted it resulted in uncontrolled temperature oscillation in the bath. Also at issue in this setup were large thermal gradients caused by the fact that the thermal tape was mounted on the exterior of the beaker which held the glycerol. To overcome this, a basic mixer was built from a computer fan, threaded rod, and small propeller. A trim potentiometer was used to control the fan speed so that the rate of mixing could be set. Once a constant temperature has been established in the bath the gage is immersed in the liquid, the temperature in the gage substrate is allowed to equilibrate, and a voltage reading is taken. This procedure is repeated for a range of temperatures , and a calibration curve is fit to these data points. An example of one of these calibration curves is presented in Figure 8a. The second calibration procedure utilized a furnace instead of a glycerol bath. The gage was placed in the furnace and it was brought to a series of temperatures between 25° C and 50° C. The voltages were recorded and a calibration curve was constructed. To check the functionality of the gages, a constant heat flux source was applied to the calibrated gage. The temperature profile and resultant heat flux data are shown in Figure 9.

Initial experiments with the thin film gages were done with isolated gages painted on scrap pieces of MACOR®. These tests were run in order to determine the optimal firing profile, gage size, and calibration technique. Once the method of construction and testing had been developed to a satisfactory level several thin film gages were painted onto a stagnation sphere model. Also, a special insert was made which could be mounted in a flat plate. This insert was 3 inches long and 0.5 inches wide, and was designed to have 12 thin film gages on the surface. Channels were cut in the side of the insert so that wires could be attached to each gage without affecting the surface of the model. A calibration curve for a stagnation sphere gage is shown in Figure 8b.

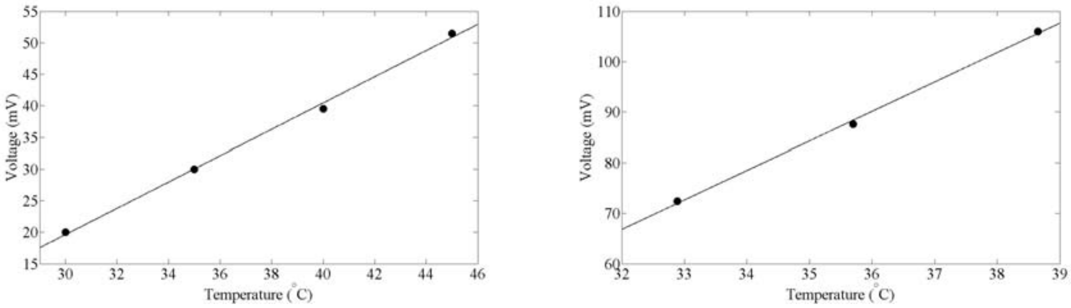

(a) Calibration of an isolated thin film gage element.

(b) Calibration of a model-mounted thin film gage.

Figure 8: Thin film calibration curves.

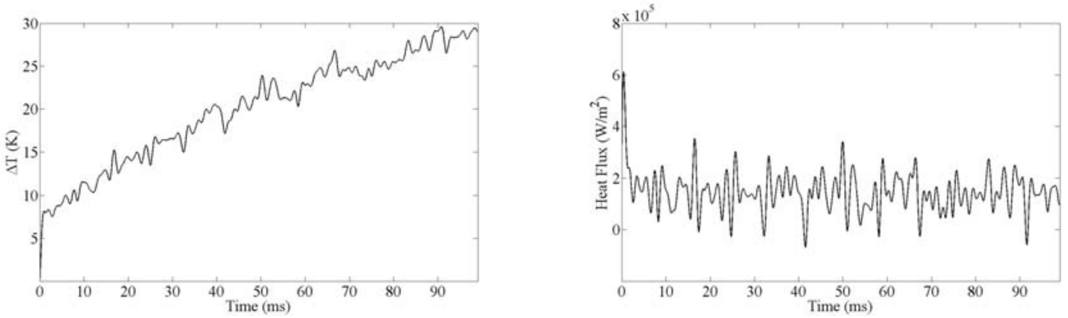

(a) Temperature history.

(b) Surface heat transfer.

Figure 9: Thin film gage data obtained from an isolated gage element exposed to a constant heat flux.

3.4 Heat flux deconvolution

Two methods were investigated to deconvolve the heat flux from the gages, both of which assumed that the gage or substrate can be modeled as semi-infinite body during the test time. The first method uses Laplace transforms to solve the heat equation, and this solution is shown in Equation 1 [38]. In order to solve this problem numerically, it is useful to use the discretized form, seen in Equation 2 (where the signal consists of $n + 1$ measurements).

$$\dot{q}(t) = \sqrt{\frac{\rho c k}{\pi}} \int_{0}^{t} \frac{dT(\tau)}{d\tau} \frac{d\tau}{\sqrt{t-\tau}} \tag{1}$$

$$\dot{q}_n = \sqrt{\frac{\rho c k}{\pi}} \sum_{i=1}^{n} \frac{T_i - T_{i-1}}{\sqrt{t_n - t_i} + \sqrt{t_n - t_{i-1}}} \tag{2}$$

where $\dot{q}(t)$ is the heat flux as a function of time, ρ, c, k are density, specific heat and thermal conductivity of the material respectively, and T is the temperature. The second method was introduced by Sanderson [25]. The solution to the diffusion equation in a semi-infinite plate exposed to a surface heat flux is represented by a convolution integral

$$\Delta T(x,t) = \int_0^t g(x, t-\tau)\dot{q}(\tau)d\tau \tag{3}$$

where ΔT is the change in temperature and $g(x,t)$ is the impulse function, given by

$$g(x,t) = \frac{\partial \Delta T(x,t)}{\partial t} = \sqrt{\frac{\alpha}{\pi k^2 t}} \exp \frac{-x^2}{4\alpha t} \tag{4}$$

where α is the thermal diffusivity and x is the junction depth. By taking the Fourier transform of Equation 3, it is possible to solve for the heat flux, such that

$$\dot{q}_n = FFT^{-1}\left[\frac{S_n}{G_n}\right] \tag{5}$$

where S_n and G_n are the Fourier transforms of the temperature signal and the impulse function respectively. While the signal is in the frequency domain, a low-pass, 4th order filter is applied to it. The cut-off is set to 20 kHz, as previous reports have shown that the gages carry little to no signal above this frequency range [25, 26, 27]. Comparison of the heat flux calculated using both these methods showed that the spectral deconvolution method resulted in a less noisy signal, in agreement with the results of Sanderson [25]. It should be noted that Sanderson's method of spectral deconvolution is specific to the thermocouples of his design. Thus, The numerical integration method was used with the thin film gages, and spectral deconvolution was used with the thermocouples.

3.5 Pressure Sensitive Paint

Fluorescent paints which are sensitive to pressure or temperature can provide full-field data over a three-dimensional surface, a significant advantage over gauge point measurements. While value of these paints has been demonstrated in numerous applications, relatively slow response time has precluded their use in many hypersonic impulse facilities. Traditionally, even "fast" pressure sensitive paints (PSPs) had response times in the range of milliseconds while test times in impulse facilities can be on the order of hundreds of microseconds. In addition, the experimental conditions in impulse facilities are typically very challenging with high shear and heat transfer rates, as well as survivability issues due to dynamic loads and particulate damage. In this study, a new PSP was used in collaboration with Innovative Scientific Solutions, Inc. (ISSI) which has a response time on the order of 30-50 μs.

Pressure sensitive paints operate through the quenching of the luminescent molecule by oxygen in the external flow. When a molecule is excited by a light source it can either emit a photon or return to its ground state without emitting a photon. This photon is typically emitted at a different wavelength than the incident light. Oxygen molecules have the effect of quenching the luminescent molecule, and causing more molecules to return to their ground state without emitting. Thus, the output intensity of the paint (assuming a constant intensity light source) will vary inversely with the partial pressure of oxygen, which should be proportional to the actual pressure of the flow if the test gas is air. For model based measurements the paint is applied to the surface of the model to be interrogated, and conventional imaging techniques are used to record the intensity distribution during the test time. Typically a long-pass filter is used on the camera in order to filter out the incident light and only capture the luminescence of the model. One issue with PSP is that the luminescence of the paint is not only a function of pressure. Factors such as paint thickness, uneven illumination, concentration of the luminescent molecule, and non-uniformities on the camera's CCD can all result in fluctuations in the recorded intensity. In order to avoid this, a ratio it taken between the image taken during the test time and an image taken with no flow over the model at a known pressure. These are designated the "wind-on" and "wind-off" images respectively.

Typical paint formulations are a mixture of the luminescent molecule and a polymer binder which is used to create the bond between the luminescent molecule and the model. The response times are dependent on the rate at which the oxygen molecules can permeate the binder before they can quench the luminescent molecules. The rate of diffusion of a gas into the binder material will be the main limit to a given paint response time. The low end of response times for typical polymer binder PSP is a few tenths of a second. When compared to the typical test times in impulse facilities capable of high velocity, high enthalpy flows such as expansion tubes (hundreds of microseconds) or reflected shock tunnels (a few milliseconds), it is obvious that these paints are grossly inadequate for capturing any of the flow structures.

As noted above, the response time of a given PSP is a function of the diffusion coefficient of the polymer binder, as well as the thickness of the paint layer. The relationship between response time τ_{diff}, diffusion coefficient D_m, and paint thickness h is typically given as:

$$\tau_{diff} \sim \frac{h^2}{D_m} \tag{6}$$

Obviously, decreasing the paint thickness will reduce the response time, but this comes with an associated decrease in signal intensity. Another method used to increase the speed of oxygen permeation is the use of porous binders. The advantage of a porous binder is that the oxygen has much easier access to the luminescent molecules, allowing the quenching to occur much faster. In addition, the effective surface area of a porous binder is much larger than its non-porous counterpart, resulting in higher radiative intensity. One downside of these binders is that since the oxygen has such easy access to the luminescent molecules, too much quenching can actually result, so that at higher pressures the signal is extremely low. It has been found that these paints are well suited for use in facilities where the static pressure is below around 20 kPa.

Development of "fast" PSP's with porous binders has been the subject of much research. The ability to create a paint with good signal-to-noise while having microsecond response time would be extremely useful not only for short duration facilities like the HET, but also to unsteady flows who's characteristic time scales are on the order of microseconds. To date, three types of fast PSP have been developed: anodized aluminum (AA) PSP, thin-layer chromatography (TLC) PSP, and polymer/ceramic PSP. AA PSP was originally developed by Asai [39] for application to cryogenic wind tunnels. AA PSP is done by anodizing an aluminum model to create a consistent honeycomb structure across the surface of the model. After this is done the luminophore can be adsorbed onto the surface of the model to create the PSP. Asai's method was further improved by Sakaue and Sullivan [40]. In this study, the response of AA PSP was compared to both TLC and polymer/ceramic PSP. They found that the best response time was given by the AA PSP, 34.8 μs. The TLC was on the same order as the AA (65.1 μs), and the polymer/ceramic was around 345 μs. The number for the polymer/ceramic is actually much higher than what is attainable with this type, as the paint was not optimized. One benefit of the AA PSP is that the thickness can be directly controlled by varying the anodization time of the model. This allows for much more direct control over the response time of the gage. Conversely, the authors of that study were unable to vary the thickness of the TLC PSP, which resulted in much less control over the paint. TLC PSP was first developed by Baron *et al.*. In this method, the luminophore is adsorbed onto the surface of a thin-layer chromatography sheet which can be purchased commercially. Baron *et al.* were able to get response times below 25 μs with their TLC PSP, and it was theorized that response times as low as 10 μs could be achieved. The drawbacks to this type of PSP are that is can only be applied to a flat plate, it does not have a large dynamic range, and it is brittle compared to the other two types (making it a poor choice for use in impulse facilities).

For this project, work was done implementing a PtTFPP porous polymer paint from Innovative Scientific Solutions Inc. (ISSI). This paint combines the properties of porous PSP with more traditional PSP to obtain fast response, while maintaining good signal at higher pressures. A coating containing luminescent molecules with a short lifetime is typically applied onto the polymer/ceramic paint in order to make the complete PSP. These types of PSP's have been used in previous studies, which were able to measure pressure fluctuation of up to 20 kHz [41]. For a much more in depth review of the development and theory behind fast response PSPs see Gregory, *et al.* [41].

Since the PSP used in has a radiative transition near 532 nm a frequency doubled Nd:YAG New Wave Research Gemini 15 laser was used for illumination. This gave the added benefit of 90 mJ/pulse illumination intensity per pulse which resulted in higher PSP signal levels. An optical diffuser was used to diffuse the laser light over the top surface model. Imaging was done using a PCO 1600 CCD camera mounted such that it imaged through the top window of the test section.

There are two different methods of collecting PSP data: radiometric and lifetime. In the radiometric method, the laser pulse occurs during the test time. The camera image acquisition is triggered simultaneously with the laser pulse, and the exposure time is long enough that a good signal level is attained. For this method the camera averages over the entire duration of the paint's luminescence. The ratio of this "wind-on" image is taken with a "wind-off" image (where there is no flow over the model) at a known pressure. This ratio should eliminate most of the effects of non-uniform lighting and paint thickness. In the lifetime method, the laser pulse again occurs during the test time, however the camera is operated in double shutter mode. The first image is taken with the specified exposure time. After the exposure time the process of reading out this image begins and, after a small delay ($\sim$ 180 ns), the second image recording begins. The limitation of this technique is that the exposure of the second image cannot be directly controlled and can vary from 22 - 208 ms. During post processing, the ratio of the two images taken during the test time is taken in order to eliminate non-uniformities in the light sheet and paint. Even though test times in the HET are on the order of hundreds of microseconds, the long exposure of the second frame was not believed to be a problem since the radiative lifetime of the paint is only a few microseconds. Thus, for most of the second exposure, the camera would only be recording background. Unfortunately, when initial experiments were run in the HET with the camera in double shutter mode it was discovered that the arrival of the driver gas in the test section results in significant natural luminescence in the gas. Even though the intensity of this luminescence is much lower than the laser intensity, it is still enough to completely saturate the second image during its exposure time. This makes the second image useless. Solutions to this issue are currently under investigation, but the data presented here were all taken in the radiative mode of operation.

To check the PSP pressure levels, static pressure measurements were made using Endevco Model 8530C-15 piezoresistive pressure transducers. These gages have a response time of about 70kHz resulting in a mean pressure measurement for comparison to the PSP to investigate the accuracy of the calibrated measurements. The gages were calibrated *in situ* in the same manner as the PSP during the evacuation of the HET. The output of the gages was also filtered through an 80kHz, low pass analogue filter in order to eliminate the effects of the resonance frequency of the gage.

3.6 Schlieren setup

When the models were first run in the HET, Schlieren imaging was used to interrogate the flowfield around the model both to look for boundary layer growth and to check for any anomalies. The Schlieren setup was a modified z-type. The modification to the typical z-type was in the form of a third mirror which turned the light. This was necessary due to size constraints from both the room size and the size of the optical table. White light was generated using a Xenon nanopulser spark gap. This spark gap created a burst of light with a pulse width of approximately 20 ns. The system was triggered using a PCB 113A26 pressure transducer. This transducer was wall mounted in the driven section and was triggered by the initial shock. It should be noted that this is a different triggering set up to that typically used in the HET. For most shots, the Schlieren system is triggered using a 113A26 transducer mounted as a pitot probe in the test section. As such, the trigger level can be set high enough that only a very short delay is necessary, and there is very high confidence that the picture is taken during the test time. For the flat plate model used in these experiments it was impossible to mount a pitot probe inside the test section. The only other option for a shock based triggering mechanism were the wave speed transducers mounted in the driven section. Due to the fact that these transducers are mounted significantly upstream of the test section there is much more uncertainty in the time between shock arrival at the wave speed transducer and the arrival of the test gas in the test section. When characterizing the run condition care was taken to ensure that good data were taken with both wave speed transducers and the pitot probe. These data were compared and it was found that adding a delay of 1.556 ms would put the light pulse in the middle of the test gas, and that the variations in elapsed time between the shock arrival and test gas arrival were small enough that this pulse would always be within the test gas. The light from the spark gap was collimated using a 4 inch, f10 mirror. The collimated light beam was then passed through the test section. After exiting the text section the mirror was then turned and focused using another 4 inch f10 mirror. The focused light was then turned again using a 2 inch turning mirror. Finally the light was fed past a razor blade which acts as the Schlieren cutoff. The camera used to capture the images was a pco.1600 CCD camera (Cooke Corporation) with a Nikon zoom lens attached to it. Images were recorded on a PC using the CamWare software provided by PCO. A sketch of the Schlieren set up with an example light beam going through the test section can be seen in Figure 10.

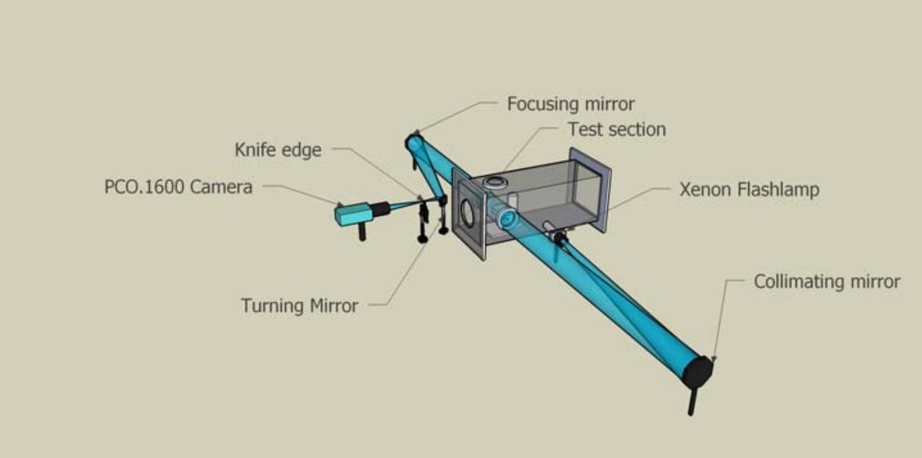

Figure 10: Sketch of Schlieren set up.

4 Models and MOC external flow calculations

4.1 Models

Six different model geometries were used in this work, flat plate, a linear compression ramp, and four curved compression ramps with differing surface equations. In addition, a one inch diameter sphere was used to verify heat transfer measurements. As will be discussed later in this document, the stagnation sphere was originally chosen due to the fact that there is an analytical solution for the heat transfer at the stagnation point.

For the flat plate, linear compression ramp, and curved compression ramp models an entirely new mounting system was required in order to limit flow blockage as well as allow for models of sufficient length. To accomplish this a new sting was required which would allow models to be top mounted instead of rear mounted. The sting was designed such that it could used the same support plate as the sting designed by Sharma so that the HET would not have to be retrofitted in order to mount the new sting. The height of the sting was designed such that the top of the tallest curved ramp model would still be within the core flow of the facility. The new sting was also designed to have a hollow center, as well as a feedthrough slot on the bottom so that wires could be fed out of the sting without being exposed to the flow. The flat plate was designed first, and two criteria were used. First, it had to be able to protect any wires from gages such that they would not be exposed to the flow and could be fed through the sting. Second, the model should be easily interchangeable so that different model geometries could be tested at a later date (since it was known that curved compression ramps would follow). As such it was decided to make the plate out of three parts, a removable leading edge, the actual flat plate, and a mounting tray. The leading edge is one inch long and was made removable so that the leading edge geometry could be maintained between models to eliminate any inconsistencies between datasets from different models. It was designed to be made out of A1 tool steel in case it was decided to harden the leading edge at a later time. Mounting to the flat plate was accomplished by two 1/4-20 socket head bolts. The flat plate was designed to be 222 mm long and 6.35 mm thick, giving the model a total length of 248 mm. It was also made such that a tripping element could be mounted at 76 mm from the leading edge. The mounting tray was designed to be the interface between the flat plate and the sting. The tray is mounted to the sting using four 5/16-18 bolts. There are two mounting locations for the sting on the tray to allow visualization of both the leading edge and the rear portions of the model through the windows of the HET. The connection between the model and the tray was initially made with four 1/4-20 bolts and designed to be 6.35 mm thick. After approximately 50 shots this tray failed during a shot. It was decided to redesign the tray to be much more sturdy, and as such it was re-designed to be 12.7 mm thick, and connect to the flat plate using four 3/8-18 bolts. Some of the interior volume of the tray was also machined away in order to make room for the 30 gage thermocouple wires to be fed through, and holes were drilled through the tray at both sting mounting locations to allow the wires to pass through the tray and into the sting. The flat plate with thermocouples, leading edge, tray, and sting are shown in Figure 11a. As mentioned earlier, a flat plate was also made which could have a strip of thin film gages mounted along its center. This model is shown in Figure 11b.

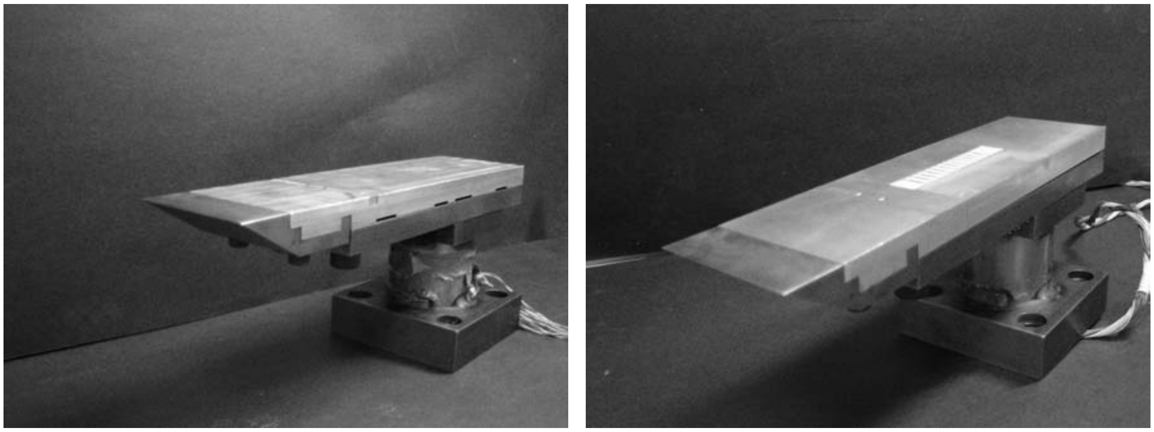

(a) Thermocouple model (b) Thin film model

Figure 11: Flat plate models

The compression ramp models (both linear and curved) were designed to mount into the same leading edge, tray, and sting as the flat plate model both to reduce the number of parts which needed to be machined and to make changing out models a quick procedure. Five different compression ramp models were built. The first to be designed was a curved compression ramp, designated as Curved25. Two different design criteria were used for this model. First, the model would start as a flat plate, with the curvature starting 83 mm downstream of the leading edge. This corresponded to the distance to the rear of the tripping element on the flat plate model, and the curved ramp was also made with a slot for trip mounting in this location. All other models designed for this project incorporated this the initial flat plate and trip slot feature. This flat plate section allows the boundary layer to develop over the model before encountering the geometry change, and ensures that the Reynolds number at the trip is consistent between the models. The radius of curvature was selected using theoretical calculations of Goertler number (based on the method described by Luca et al. [14]). Using this method, the Goertler number over Curved25 was calculated to vary between 12 and 15. This magnitude was chosen based on the results of Ciolkosz and Spina [42] who showed that in a compressible flow Goertler vortices were observed between Goertler numbers of 6 and 13. Since increasing Mach number should have a stabilizing effect on the flow it was decided that the curved ramps should have Goertler numbers on the high end of this range. This resulted in an overall turning angle of 25 degrees for this model. This model was instrumented with five coaxial thermocouple gages along its center. Figure 12a shows the Curved25 model with thermocouples mounted in it.

The second curved ramp model, denoted as Curved16, was designed to recreate the ramp used by Donovan *et al.* [9] to investigate the effects of wall curvature in a Mach 2.86 flow. Again, the model was designed with an initial flat section in order to match the Reynolds number at the trip for each model. The flat section is followed by a curved segment with a turning angle of 16 degrees, followed by a final, linear section. This model was instrumented with 14 total thermocouples, ten along the center of the models and four slightly offset from the center axis. In addition, four pressure gages were mounted along the center axis of the model at the same location as the off-center thermocouples. Figure 12b shows Curved16.

The third curved compression model was designated as Curved10. This model was designed to maintain the same constant curvature design of the first two models, while having a much larger radius of curvature. This resulted in a lower turning angle of 10.5 degrees. This model was instrumented with 10 thermocouples along its center axis. The linear compression ramp, denoted as Linear10, was designed for comparison with the Curved 10 model. It had the same overall turning angle as Curved10, but it was designed as a simple wedge starting after the tripping element. This model was instrumented with nine thermocouples, 5 mounted on the center line and 4 mounted off-center. Additionally, it was designed so that 4 pressure gages on the center line at the locations of the off-center thermocouples. Figures 13a and 13b show the Curved10 and Linear10 models respectively.

The final model used in this project was the Cubic1 model. The need for this model arose after it came to the authors attention that all three previous curved compression ramps had surface equations which were described by quadratic function. It was decided that it would be beneficial to have a model with a drastically different surface equation in order to truly investigate the effects of surface geometry on the boundary layer characteristics. The only constraint on the surface equation was that it have zero angle at the origin and that its final height be within the core flow of the facility. With these constraints in mind a surface equation was created in Excel, and a series of surface points were generated. These data were used to create the surface in a solid modeling program, and the model was cut by a CNC machine using this model. The cubic surface equation introduces two interesting characteristics to the model. This model has the highest overall turning angle, 32 degrees, and has a variable radius of curvature. It was instrumented with nine thermocouples along its center axis. Figure 14 shows the Cubic1 model.

As mentioned earlier in this section, each model is designed such that a strip of protuberances can be mounted 83 mm behind the leading edge. Four different roughness geometries were used in this study. All four were based on the work of Berry *et al.* [43] in their work developing trips for the Hyper-X vehicle. The first roughness used was a basic diamond shaped geometry with the points of the diamonds oriented in the flow direction. The elements had a length, width, height, and separation of 2 δ. The other three roughness geometries were all variations of triangles. Designs for these three trips were based off of trips 2a, 2b, and 2c from the work of Berry *et al.*, and were designated with these same labels in this work. The only difference between these trip designs and the ones used by Berry were the roughness elements for this work were scaled by 2 δ rather than just δ. Sketches of the roughness geometries are shown in Figure 15. It should be noted that these represent an individual roughness, while a strip of roughness elements was installed in the models. Images of the actual roughness element strips can be seen in Figures 16, 17, and 18.

Finally, a one inch diameter sphere model was used to verify both the thermocouple and thin film gages. When choosing the sphere diameter it was desirable to choose a size which would allow easy mounting of the thermocouple, and maximize the heat flux (to maximize the signal). Additionally, it was necessary that MACOR®rod was available in the diameter desired such that a thin film model could be constructed of the same size. Since stagnation point heat transfer decreases with increasing sphere radius, a one inch sphere was chosen as it was determined that any smaller would make thermocouple mounting as

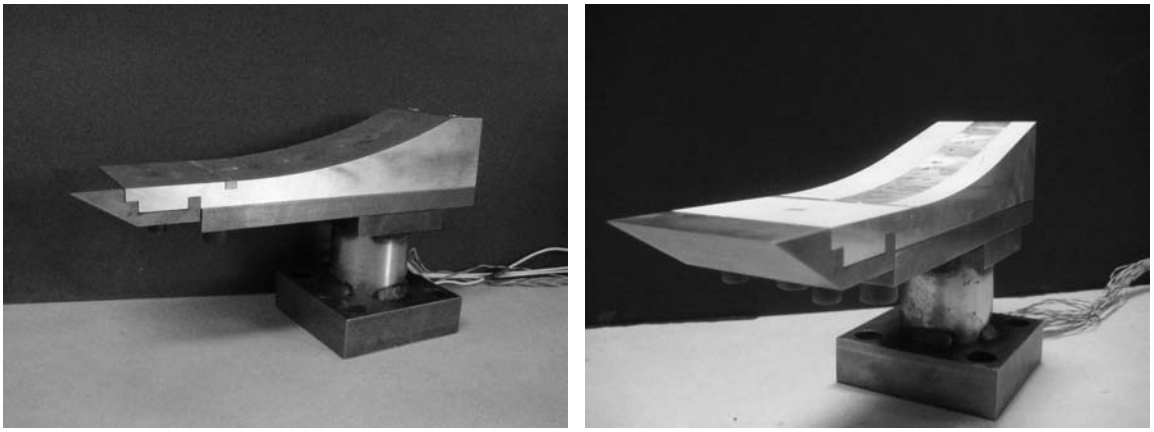

(a) (b)

Figure 12: (a) Curved25 (b) Curved16

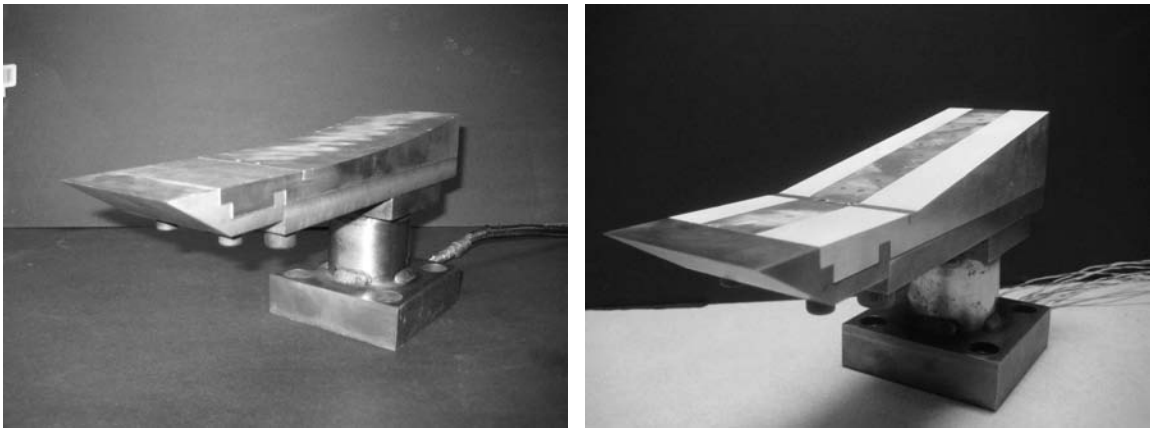

(a) (b)

Figure 13: (a) Curved10 (b) Linear10

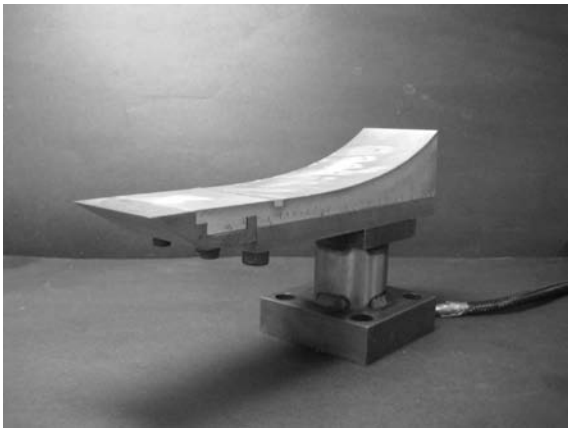

Figure 14: Cubic1

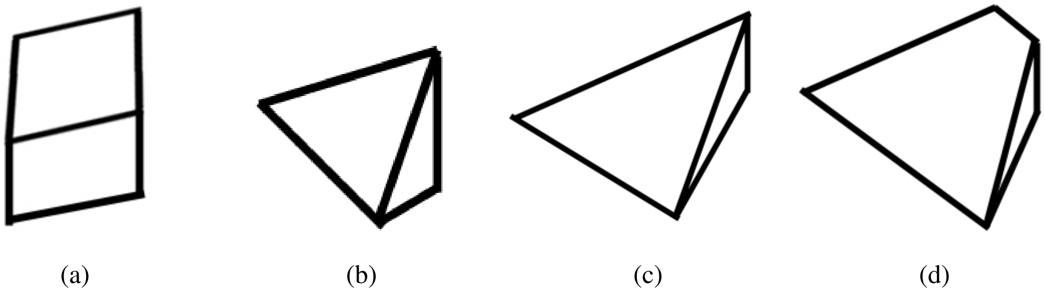
(a) (b) (c) (d)

Figure 15: (a) Diamond roughness (b) Roughness 2a (c) Roughness 2b (d) Roughness 2c

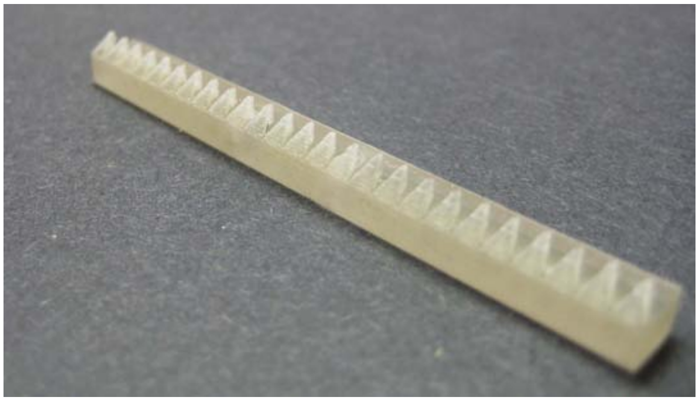

Figure 16: Triangle roughness 2a

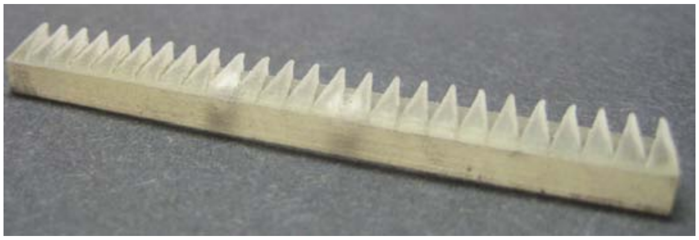

Figure 17: Triangle roughness 2b

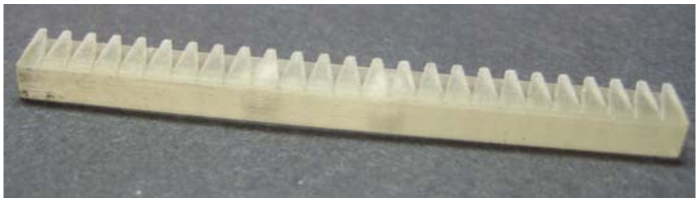

Figure 18: Triangle roughness 2c

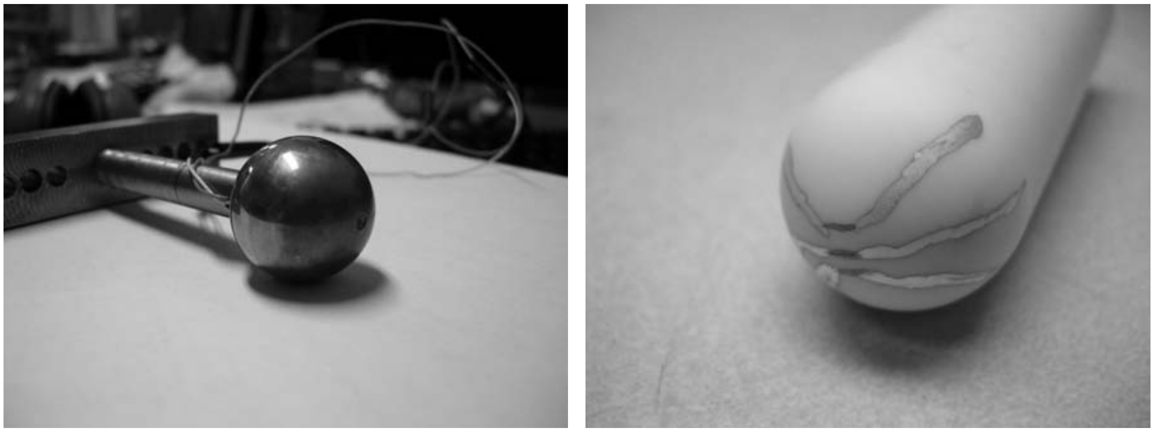

(a) Steel stagnation sphere (b) MACOR®stagnation sphere

Figure 19: Stagnation sphere models

well as sting mounting difficult. Due to the fact that it was shot tested, the sting designed by Sharma [18] was used as the mounting base in both the thermocouple and thin film stagnation sphere designs. The thermocouple stagnation model was constructed from a one inch ball of basic carbon steel. A 0.098 inch through hole was drilled in the sphere for thermocouple mounting. A blind hold was drilled and tapped for 3/8-18 on one side of the sphere (concentric to the thermocouple hole) for mounting. The mounting rod was a 0.375 inch diameter piece of carbon steel externally tapped for 3/8-18 on both sides. This was designed to be threaded into a mounting plate which can be mounted to the sting designed by Sharma. The corresponding thin film model was made from a one inch diameter rod of MACOR®. One face of the rod was machined such that it would have a one inch diameter spherical nose radius. Two channels were cut down the sides of the rod in order to allow the wires which were connected to the gage to be fed through the mount. The rod was sleeve mounted to the same sting used for the thermocouple model. The sleeve was designed to have the same inner diameter as the rods outer diameter (allowing the rod to have a sliding fit with the sleeve). Three holes were drilled at equal spacing around the sleeve and tapped with 8-32 threads. These holes were used for set screws which were used to hold the rod in place during the shot. An additional hole was drilled in the sleeve to allow the wires to be fed through the sleeve. Also, when the MACOR rod was mounted in the sleeve a rubber stopper was inserted behind the rod. This rubber stopper was intended to be a cushion should the set screws fail during the shot so that the rod would not forcibly impact the metal sleeve mount. An image of both the steel and MACOR®stagnation models can be seen in Figure 19.

4.2 Freestream conditions

For this project, three test conditions with different stagnation enthalpies were selected. Inviscid, perfect gas dynamic calculations are used to predict test gas conditions. Previous to the beginning of this experiment the HET had two well characterized run conditions, which

Table 1: High-density run conditions

Test Gas	Accelerator Gas	M_∞	T (K)	h_0 (MJ/kg)	Re/m	Static P (kPa)
Air	He	6.08	564.1	4.75	2.65X10^6	4.30
CO2	He	6.94	626.3	4.20	2.75X10^6	3.84
Ar	He	6.23	582.5	4.23	1.98X10^6	4.07

are now designated as Air-5 and Air-6. Both of these run conditions are low Reynolds number and low density conditions. Since the HET has the ability to access a range of run conditions it was decided to investigate run conditions that would have an increased Reynolds number and density than those of the Air-5 and Air-6 cases. Three high density run conditions were initially studied, and their properties are shown in Table 1.

While both the Reynolds number and density of these shots were in the desired range, they displayed extremely high levels of free stream noise throughout the test gas, making them unusable. An example pitot trace from one of these shots (centered in the time around the test gas) can be seen in Fig 20. It is believed that the noise in the test gas is a function of the ratio of the gas density between the driver and driven sections [44]. Thus, the only way to reduce noise is to reduce the driven pressure (since the burst pressure of the driver is set by the knife blades and diaphragm). Unfortunately, reducing the driven pressure (and therefore the accelerator pressure) to maintain the same run condition will result in much lower

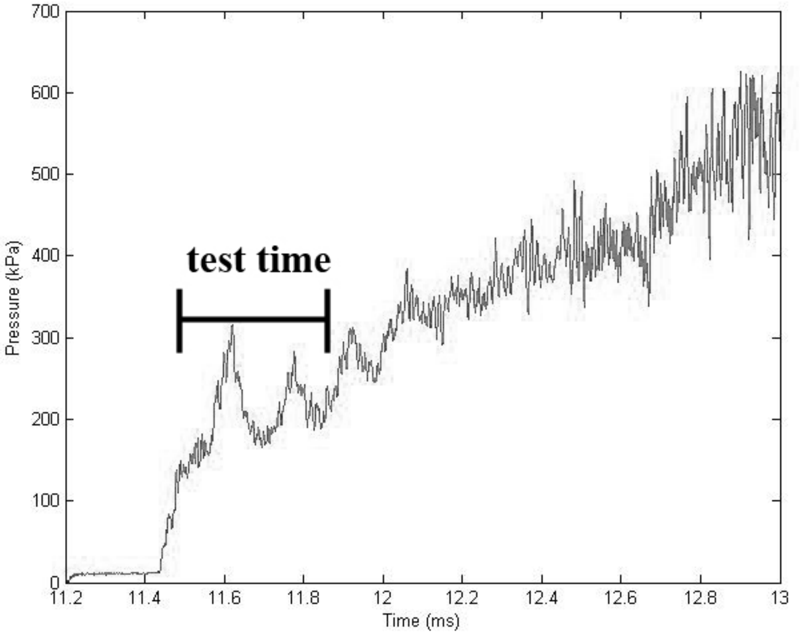

Figure 20: Pitot trace of unsuitably noisy high density test condition. This condition was not used for experiments

Table 2: Theoretical parameters for HET run conditions.

Condition	Air 4	Air 5	Air 6
Mach number	5.12	7.45	5.73
Static temperature, K	676	642	909
Static pressure, kPa	8.13	0.77	1.86
Velocity, m/s	2664	3779	3457
Density, kg/m^3	0.042	0.004	0.007
Test time, μs	361	163	242
Unit Reynolds number, $1/m$	3.42E6	0.50E6	0.63E6
Stagnation Enthalpy, MJ/kg	4.08	7.65	6.70
Initial Pressures, kPa			
Driver section	2500	2500	2500
Driven section	6.0	1.5	1.2
Expansion section	0.08	0.02	0.07

densities, and therefore lower Reynolds numbers. In order to try to alleviate this problem, it was decided to run the lower driven and accelerator pressures, but change the accelerator gas to match the test gas. This resulted in a higher Reynolds number and density, but comes with an associated decrease in Mach number due to the decreased sound speed ratio across the driven and accelerator sections. Trial shots were run at this new condition using air as both test and accelerator gas, and the pitot traces indicated a long, stable test time. Another parametric study was undertaken to determine a run condition with a suitably high Mach number and acceptable Reynolds number. A new run condition, designated Air-4, was found that satisfied both requirements. Its parameters are presented in Table 2 along with those of Air-5 and Air-6. The Mach number and enthalpy of Air-4 lie on the mid and low ends of the tubes capabilities respectively. Air-5 is a variation of the original main run condition in the tube. It was re-classified from Air-1 to Air-5 when the burst pressure of the primary diaphragm was lowered, which resulted in a slight change in the run condition. Air-5 is a low density, low unit Reynolds number condition, and has a Mach number and enthalpy that lie on the higher end of the tubes capabilities. For this condition helium is used as the accelerator gas. Air-6 is also a low density, low unit Reynolds number condition, but it's Mach number and enthalpy lie in the mid-rage of the tubes capabilities. Air-6 utilizes helium as the accelerator gas.

5 Method of Characteristic Predictions

The method of characteristics (MOC) was used to calculate the external flows over the compression surfaces and the ensure that the shock formed over the ramps would not interact with the boundary layer. In an effort to understand the wave patterns from the surfaces investigated, a two dimensional MOC code was written to predict wave behavior as well as shock location and shape. The code is entirely inviscid, as such, no effects of the boundary layer are considered. This section outlines two different methods for calculating the shock location and shape: an isentropic method, and a non-isentropic method.

5.1 State calculations

The code reads in a data file containing the x and y locations of the surface of the model, and takes user inputs for the freestream Mach number, temperature and pressure. The code then solves for surface Mach number, pressure, and temperature using isentropic turning theory. The relative turning angle of each segment is numerically calculated, and by implicitly solving the Prandtl-Meyer function (Equation 7) with a Newton-Rhapson Method, the surface Mach number is obtained.

$$\nu = \left(\frac{\gamma+1}{\gamma-1}\right)^{1/2} tan^{-1}\left[\frac{\gamma-1}{\gamma+1}\left(M^2-1\right)\right]^{1/2} - tan^{-1}\left(M^2-1\right)^{1/2} \tag{7}$$

ν is the Prandtl-Meyer angle, γ is the ratio of specific heats, and M is the Mach number. With the Mach number being known, the isentropic flow relations can thus be used to calculate the corresponding pressures, temperatures, and velocities. Each ramp is divided up into 10,000 equally spaced points to create adequate resolution of the local turning angle.

5.2 Methodology

5.2.1 Isentropic

Along a curved ramp, C^+ characteristics will be the mechanism for turning the flow and increasing the temperature and pressure. At the intersection of the first two body C^+ characteristics a shock will necessarily form. Thompson [45] outlines a procedure to predict the shape of this location for weak waves. Figure 21 illustrates two C^+ characteristics interacting.

Thompson shows that for weak waves (i.e. small turning angles) that $\epsilon_1 \approx \epsilon_2$ and that the error involved in this approximation is proportional to the square of the turning angle, δ^2. We thus implement this procedure in MATLAB and solve the flow field, progressing downstream. The shock will be formed by the intersection of the C^+ characteristics from the freestream and the C^+ characteristics from the body. The entire shock structure is found by extending the line from previous characteristic interaction until it intersects the next C^+ characteristic from the body. A schematic for this is shown in Figure 22.

5.2.2 Non-isentropic

For the non-isentropic case the procedure is nearly the same as the isentropic case, however, the shockwave angle is solved for by implementing the oblique shock relation given by Equation 8.

$$tan\left(\delta\right) = 2cot\left(\theta\right)\left(\frac{M_1^2 sin^2\theta - 1}{M_1^2\left(\gamma + cos2\theta\right) + 2}\right) \tag{8}$$

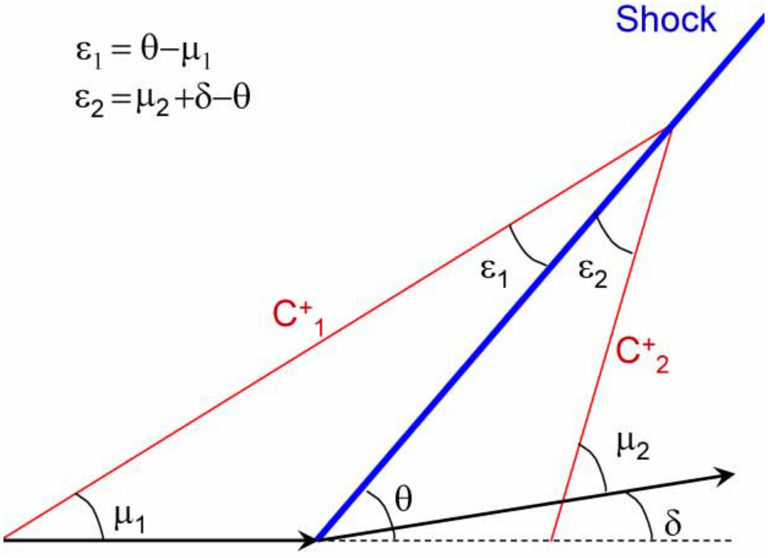
Shock
$\varepsilon_1 = \theta - \mu_1$
$\varepsilon_2 = \mu_2 + \delta - \theta$
ε_1
ε_2
C^+_1
C^+_2
μ_2
θ
μ_1
δ

Figure 21: A depiction of the interaction of two C^+ characteristics, which form a shock. Flow is from left to right.

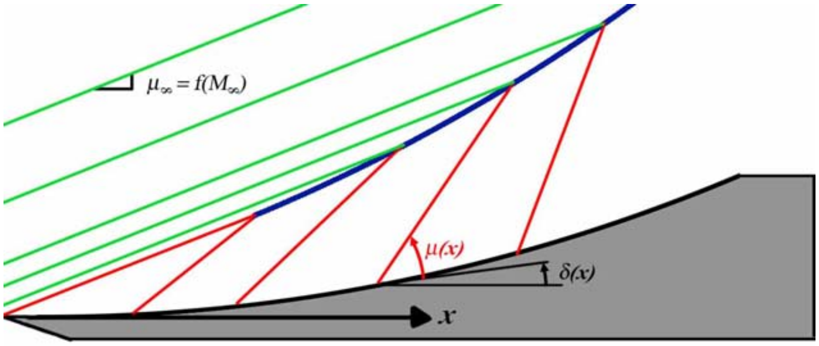
$\mu_\infty = f(M_\infty)$
$\mu(x)$
$\delta(x)$
x

Figure 22: A schematic of the flowfield and the different C^+ characteristics in it. Flow is from left to right. Green characteristics are from the freestream, red characteristics are from the body. The blue line is the shock wave.

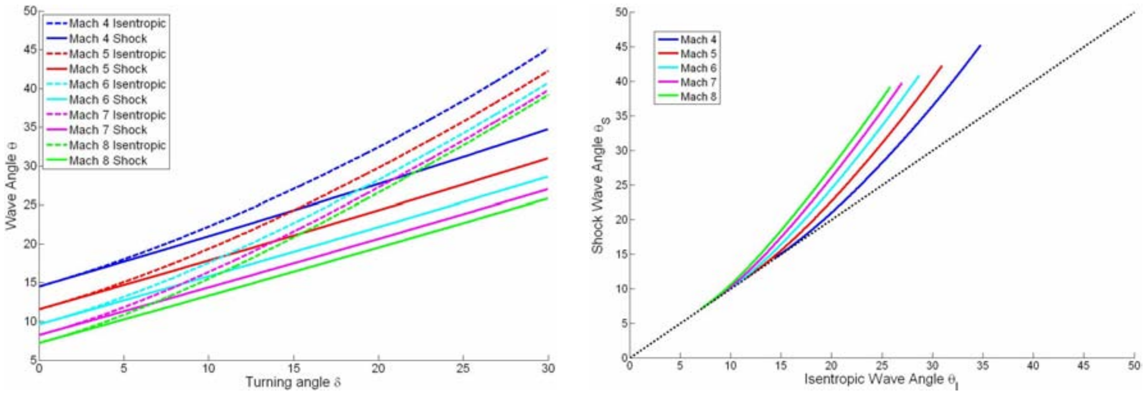

(a) (b)

Figure 23: (a) For varying Mach numbers typical of HET operation the isentropic wave angle, θ_I, and the non-isentropic wave angle, θ_S, are plotted as functions of the turning angle. (b) The non-isentropic wave angle is also plotted as function of the isentropic wave angle. The dotted line has a slope of 1 to illustrate deviations.

The turning angle used is that of the absolute turning angle with respect to the freestream. Physically this assumption means that information from the surface is transfered along the characteristic until it intersects the shock. Figures 23(a) and (b) illustrate deviations resulting from the isentropic assumption versus the non-isentropic assumption.

Figures 23(a) and (b) clearly indicate that non-isentropic wave behavior becomes important for reasonably small turning angles.

5.3 Ramp results

Figures 24(a) and (b) show the resultant shock shape over the Curved25 for Mach number of 5.12 and 7.42 respectively. The surface is shown by the bold black line, characteristics from the surface are shown by the red lines, the isentropic wave is illustrated by the green line, and the non-isentropic wave is illustrated by the blue line.

Figures 25(a) and (b) show the resultant shock shape over the Curved16 model for Mach numbers of 5.12 and 7.42 respectively. The color scheme is the same as in Figure 24.

For both models, we observe that near the beginning of the shock formation the isentropic and non-isentropic solutions exhibit good agreement, as we would expect for these low turning angles. With increasing turning angle the non-isentropic wave deviates, and as we would expect from Figure 23(a) is larger than the isentropic turning angle. Thus, the more realistic entropy increase due to non-isentropic waves tends to increase the distance between the wave and the body.

5.4 Convergence

While 10000 points are used for each model, the number of characteristics, N, used to compute shock location can be varied (i.e. only certain elements may have a characteristic). A convergence study is preformed for the M = 5.12, curved ramp case. The metric by

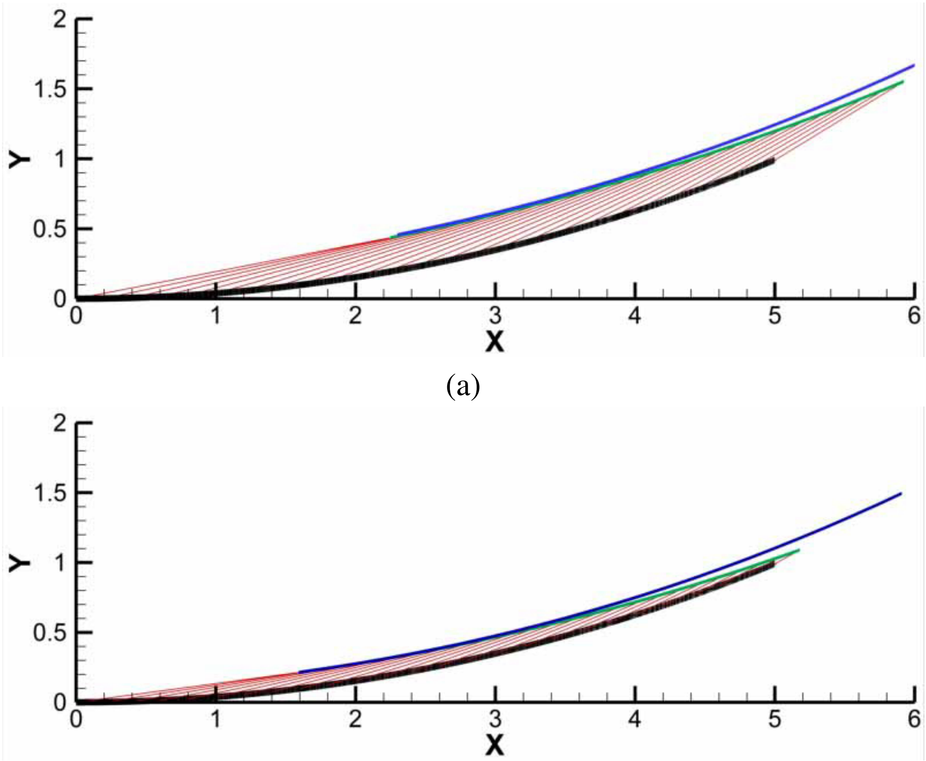

(a)

(b)

Figure 24: Shock wave behavior for the Curved25 at Mach numbers of (a) 5.12 and (b) 7.42. x and y units are in inches.

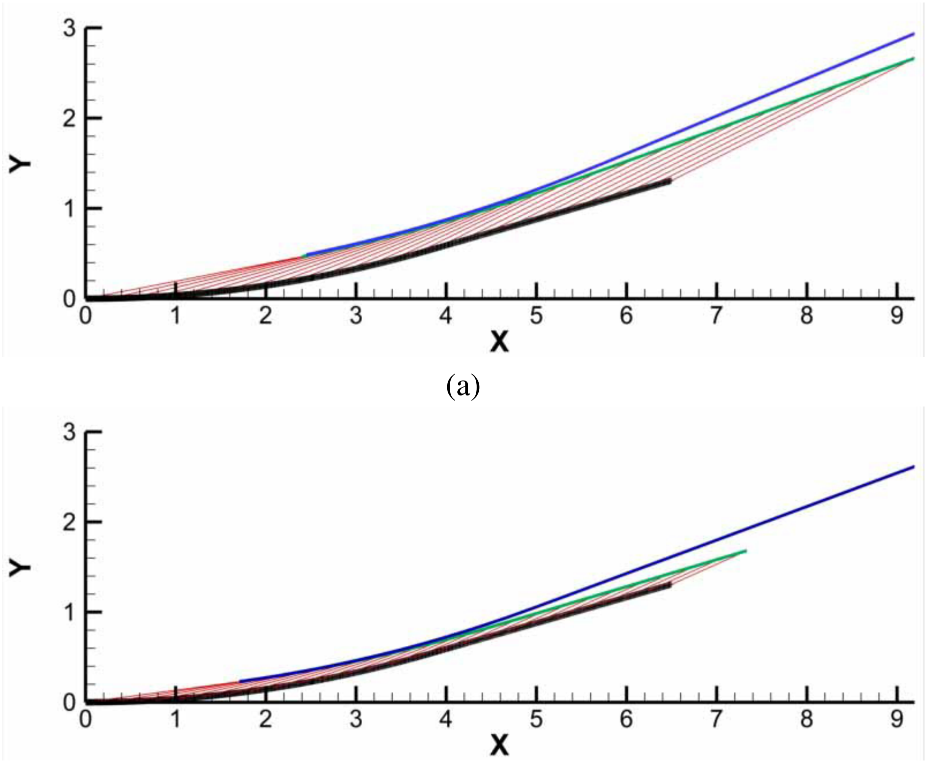

(a)

(b)

Figure 25: Shock wave behavior for the Curved16 model at Mach numbers of (a) 5.12 and (b) 7.42. x and y units are in inches.

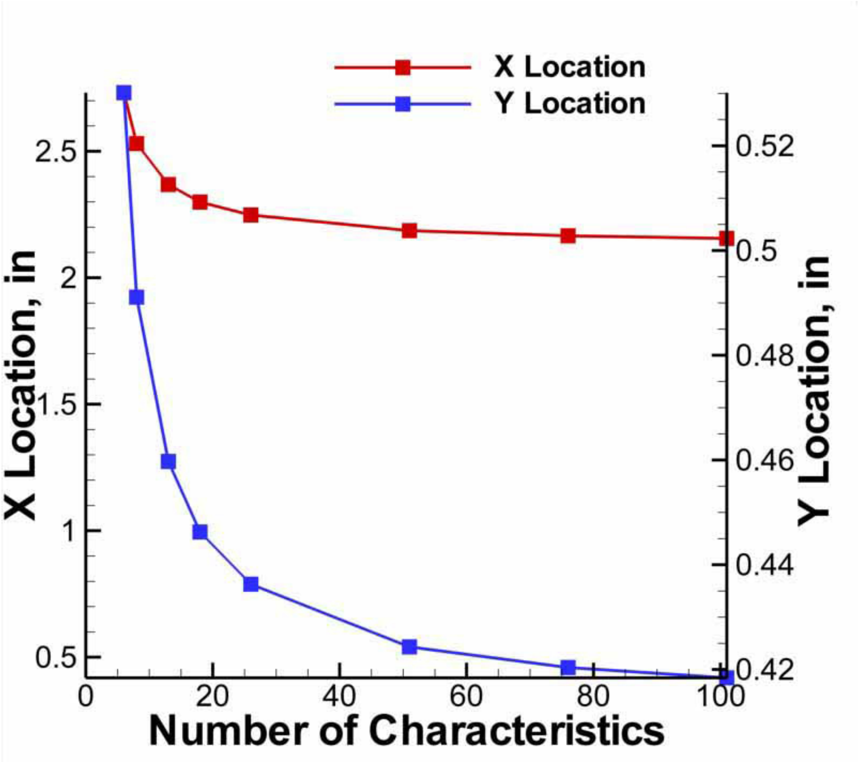

Figure 26: The x and y locations of the shock formation are plotted versus the number of characteristics used on the curved ramp model at M = 5.12.

which convergence is assessed is the location of the shock formation. This plot is presented in Figure 26.

We see that the code converges for approximately 100 characteristics, thus showing that for large enough N, the shock wave will be independent of the number of characteristics.

6 Validation of gages

Initially, data were taken with the stagnation and flat plate models, both of which have corresponding analytical models to predict the heat transfer [19, 20]. The task of predicting the heat transfer at the stagnation point in high speed flows was first undertaken by Fay and Riddell [46]. By treating air as a binary mixture of molecules and atoms and limiting themselves to the stagnation point they showed that the boundary layer equations can be reduced to a set of self-similar equations, even when accounting for arbitrary chemical reaction rates. This result allowed them to find numerical solutions for the stagnation point heating even when the boundary layer was not in a frozen or equilibrium condition. Additionally, they were able to run a parametric study using their numerical solution over a wide range of altitudes and flight speeds when assuming either an equilibrium or frozen boundary layer. They were able to perform curve fits to these data and develop analytical solutions for the heat flux for both the frozen and the equilibrium boundary layer. One more variable that was taken into account in the study was the effect of wall catalysis. For the case of the equilibrium boundary layer wall catalysis is a non-issue as it is not possible for any further chemical reactions to occur at the wall. Alternatively, when the flow is frozen, wall catalysis can have a significant effect on the stagnation point heat transfer. When developing their equations, Fay and Riddell considered two different wall catalysis conditions, non-catalytic and fully catalytic. In the non-catalytic case there are no reactions at the wall, and the flow maintains the same concentration of molecules and atoms as it did throughout the boundary layer. The fully catalytic condition indicates that there is full recombination at the wall, and therefore the fluid at the stagnation point consists only of molecules. It is important to note that in all these calculations, the gas was air, and therefore they are not valid for other gases.

Equilibrium boundary layer:

$$q = 0.94(\rho_w\mu_w)^{0.1}(\rho_s\mu_s)^{0.4} \times \left\{1 + (Le^{0.52} - 1)(h_D/h_s)\right\}(h_s - h_w)\sqrt{(du_e/dx)_s} \tag{9}$$

Frozen boundary layer, non-catalytic wall:

$$q = 0.94(\rho_w\mu_w)^{0.1}(\rho_s\mu_s)^{0.4} \times \{1 - (h_D/h_s)\}(h_s - h_w)\sqrt{(du_e/dx)_s} \tag{10}$$

Frozen boundary layer, fully catalytic wall:

$$q = 0.94(\rho_w\mu_w)^{0.1}(\rho_s\mu_s)^{0.4} \times \left\{1 + (Le^{0.63} - 1)(h_D/h_s)\right\}(h_s - h_w)\sqrt{(du_e/dx)_s} \tag{11}$$

There has been some work performed after the development of these equations to simplify them so that they may be applied more easily, and to extend them to different gases. Sutton and Graves [47] developed an equation for the equilibrium boundary layer that can be used to calculate the stagnation point heat flux for an arbitrary test gas. Their equation is given in Equation 12.

$$\dot{q} = K\sqrt{\frac{p_s}{R}}\,(h_{0,e} - h_w) \tag{12}$$

Table 3: Comparison of experimental heat transfer with theoretical predictions.

	Experimental heat flux	Sutton and Graves	Filippis
Air-4	7.85±0.63 MW/m^2	6.29 MW/m^2	6.40 MW/m^2
Air-5	7.74±0.62 MW/m^2	5.41 MW/m^2	6.15 MW/m^2
Air-6	8.50±0.68 MW/m^2	5.66 MW/m^2	6.28 MW/m^2

Where K is a constant based on the gas composition. Another expression was computed by Filippis in order to extend the predictive range of the theory from a maximum flow enthalpy of 23 MJ/kg to 39 MJ/kg [48]. This is shown in Equation 13.

$$\dot{q} = 90\sqrt{\frac{p_s}{R}}\left(h_{0,e} - h_w\right)^{1.17} \tag{13}$$

Though the experiments done here are within the 23 MJ/kg limit, the two equations still yield different results, and thus the experimental measurements were compared against both theoretical predictions.

Theoretical predictions for laminar flat plate heat transfer were calculated with the reference enthalpy method of Simeonides [49], shown in Equation 14.

$$\frac{\dot{q}_w L P^{2/3}}{\mu_e c_p\left(T_{rec} - T_w\right)} = C\left(\frac{p_e}{p_e}\right)^{(1-n)}\left(\frac{T_e}{T^*}\right)^{(1-n)}\left(\frac{\mu^*}{\mu_e}\right)^{n}\left(\frac{u_{main}}{u_e}\right)^{(1-2n)}\left(u_{grad}\frac{L}{u_e}\right)^{n}\mathrm{Re}_{e,L}^{(1-n)} \tag{14}$$

and predictions of turbulent flat plate heat transfer were made using the Van Driest II method [50], an explanation of which can be found in Sharma's thesis [18].

Thermocouple data were taken at three different test conditions with calculated stagnation enthalpies from 4.09 to 7.52 MJ/kg (listed in Table 2). Figures 27, 28, and 29 show the comparison between the temperature rise and the pitot pressure trace over a time period which encompasses the test gas. In all three plots, the temperature trace shows the arrival of the initial shock, accelerator gas, and contact surface, and the response time compares very well with the pitot pressure histories. The response time of the thermocouple gage was found to be sensitive to the degree of sanding used to create the thin thermocouple junction.

The experimentally measured heat fluxes for each condition, and the theoretical predictions are listed in Table 3. It is evident that in every case the heat transfer is under-predicted by theory. This is consistent with the results obtained by Marineau and Hornung while calibrating a new conical nozzle in the T5 facility [51]. The equation developed by Filippis provides the best prediction of the heat flux, with a 23% deviation in Air-4, a 26% deviation in Air-5, and a 35% deviation in Air-6.

For the thin film gages, initial data were taken with the HET operating as a shock tube. The stagnation region gage was able to capture the initial shock and subsequent temperature rise very well. The temperature trace is shown in Figure 30 and calculated heat transfer

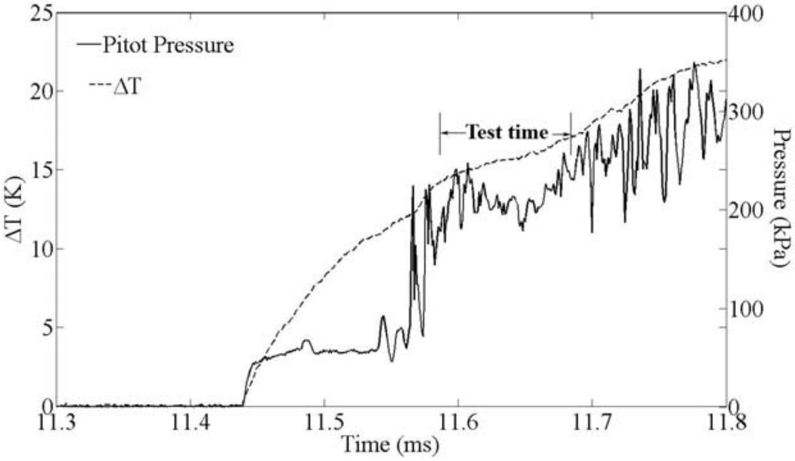

Figure 27: Air-4 temperature rise vs. pitot pressure.

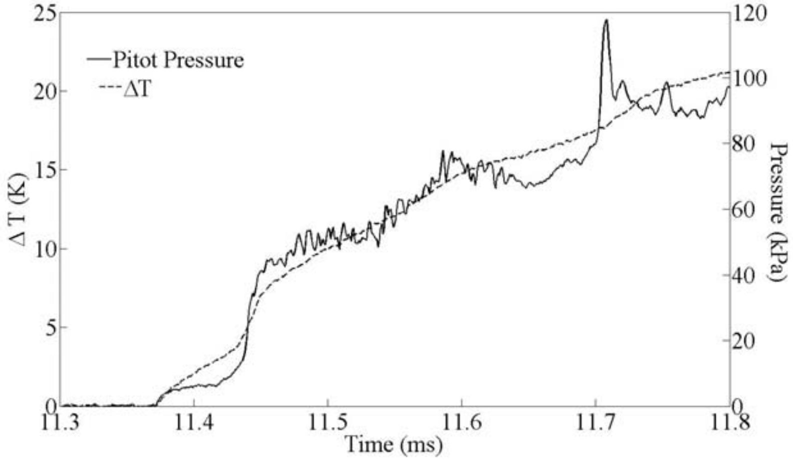

Figure 28: Air-5 temperature rise vs. pitot pressure.

data are shown in Figure 31. Shock arrival can be seen at 11.31 ms, referenced from the primary diaphragm rupture. The temperature history is presented unfiltered. Low-pass filtered data were used for the subsequent heat transfer calculation. The average heat flux over the steady state temperature rise is 2.95 MJ/m^2.

Thin film gage survival at the stagnation point was zero under expansion tube conditions. When measured between successive shots, changes in resistance were typically on the order of 500%. This is most likely due to gage damage from the high temperatures, shear forces, and debris that the model is exposed to during an experiment. This large resistance change calls into question the accuracy of any calibration curve for the gage. Since it is not known at what point in the experiment the gage was damaged, it is impossible to say if the calibration curve was still accurate during the test time. A second problem arose due to the exposed connection between the silver leads and the wire connection. Since this connection was exposed to the flow it had significant effects on the signal-to-noise ratio, decreasing confidence in the measurements.

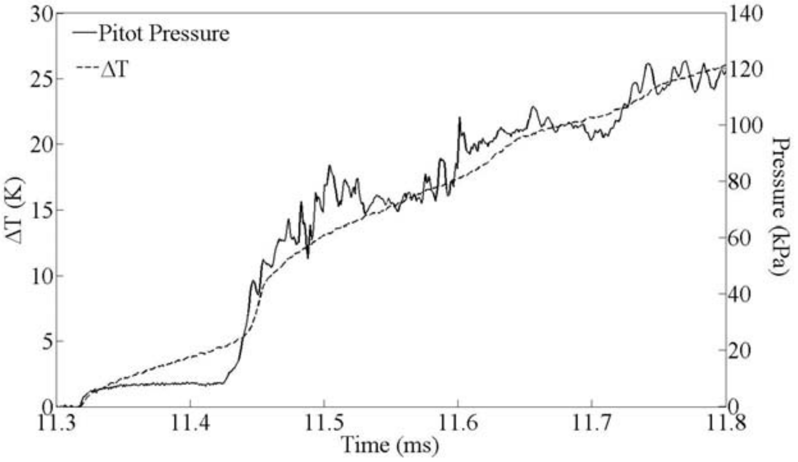

Figure 29: Air-6 temperature rise vs. pitot pressure.

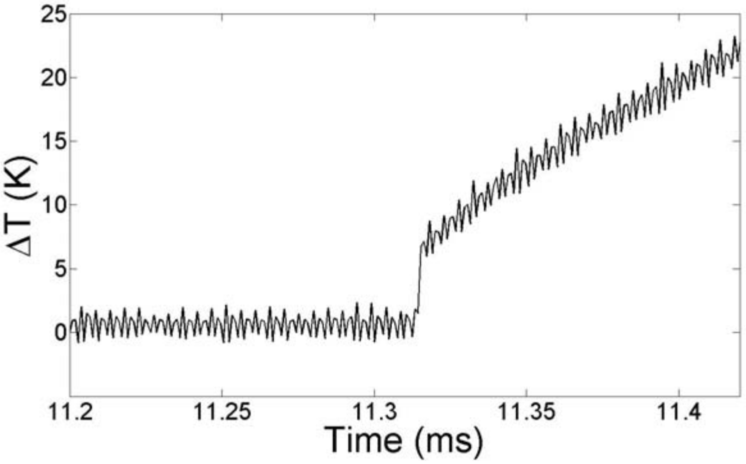

Figure 30: Thin film raw temperature history.

6.1 Unsteadiness

In the initiation of any flow over a model, there is a finite time over which the flow must establish itself over the surface of the model. During this establishment time, the flow is denoted as “unsteady” and this may have noticeable effects on the properties at the surface of the plate (including the heat transfer). The relaxation of a flow to a steady state happens in two different regimes, the external, inviscid region, and the viscous, boundary layer region. The inviscid region relaxes to steadiness quickly, within one flow length of the model. The boundary layer relaxes more slowly due to the viscous processes which dominate the flow in this region [52]. In a recent study by Marineau, et al. [53] in the T5 facility at Caltech, it was found that at their high enthalpy condition a steady state was not achieved over the

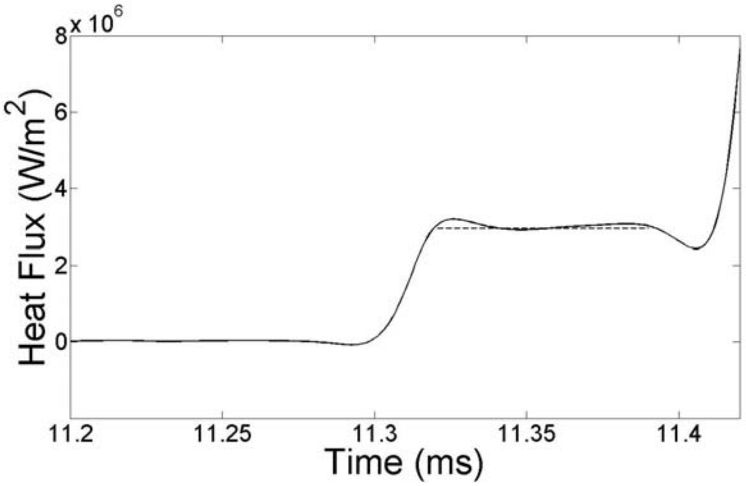

Figure 31: Thin film heat transfer during accelerator gas (dotted line indicates test time)

model. The result of this was that the heat flux measured in these unsteady cases was higher than theory. This prompted an investigation into unsteadiness in the HET. Gupta [52] performed an analysis on the time required for the boundary layer to relax to steadiness on a flat plate in an expansion tube. Two different modes of expansion tube operation were identified, the Mirels limit and the Blasius limit. In the Mirels limit, the transmitted shock from the rupture of the secondary diaphragm and the contact surface are so close together that the time between their arrivals goes to zero. In the Blasius limit the transmitted shock and the contact surface are sufficiently far apart that the time between them can be said to go to infinity. In all three run conditions used here it is reasonable to assume we are in the Blasius limit. In this regime, a Blasius boundary layer is established over the flat plate during the time in which the accelerator gas is passing over it. With the arrival of the contact surface, this boundary layer is washed away, and a new boundary layer consisting of test gas must be formed. During this transition, there is a finite amount of time when the boundary layer will consist of both accelerator and test gas while it is simultaneously relaxing to a steady state. Gupta performed a series of numerical calculations and determined that there was a critical value for the non-dimensional parameter α after which steady boundary layer flow would be established in the test gas. The non-dimensional parameter is defined as:

$$\alpha = \frac{L}{u_e t} \tag{15}$$

Where t is the time coordinate beginning with the arrival of the contact surface. Gupta determined that at a value of $\alpha = 0.3$ the boundary layer would have relaxed to a state where it is completely composed of test gas and is steady. Since the external flow velocity of the run conditions can be estimated using the inviscid perfect gas code, it is possible to compute the theoretical time to reach steadiness at each thermocouple location along the plate. When analyzing all flat plate and ramp data this time was taken into account, and heat flux levels were only averaged after theoretical time to steadiness had passed.

Gage comparison was also done with the flat plate models. Figures 32, and 33 show the comparison of the thin film data to the thermocouple data for the Air-4 and Air-6 run con-

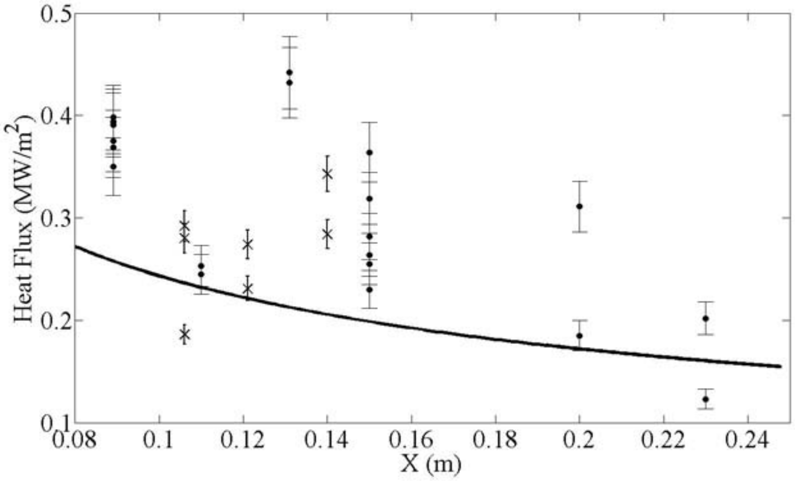

Figure 32: Comparison of thin film (×) and thermocouple (•) heat flux data in Air-6 (leading edge at x=0). The solid line is the prediction from Simeonides.

ditions, we were unable to collect flat plate data for the Air-5 condition. Both conditions show good agreement between the thermocouple and thin film gages near the leading edge, and measurements are in reasonable agreement with theoretical predictions [49]. Table 4 shows the differences between all the gages and theory on the flat plate. This shows the relatively good agreement between the two gage types and with predictions.

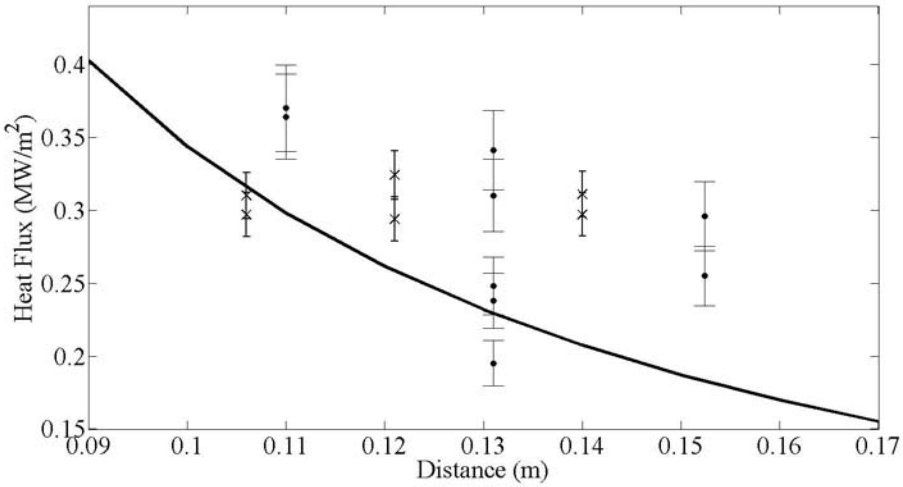

Figure 33: Comparison of thin film (×) and thermocouple (•) heat flux data in Air-6 (leading edge at x=0). The solid line is the prediction from Simeonides.

Table 4: Comparison of experimental and theoretical flat plate data with percent differences from theory.

x,mm	Air-4 Experimental (MW/m^2)						Air-6 Experimental (MW/m^2)				
Thermocouple gages											
89	0.40	0.39	0.39	0.38	0.37	0.35	-	-	-	-	-
	54%	53%	52%	45%	43%	36%	-	-	-	-	-
111	0.25	0.25	-	-	-	-	0.37	0.36	-	-	-
	9%	6%	-	-	-	-	24%	22%	-	-	-
131	0.44	0.43	-	-	-	-	0.34	0.31	0.25	0.24	0.20
	107%	102%	-	-	-	-	47%	34%	7%	3%	16%
152	0.36	0.32	0.28	0.26	0.26	0.23	0.30	0.26	-	-	-
	83%	61%	42%	33%	28%	16%	58%	36%	-	-	-
Thin film gages											
106	0.29	0.28	0.19	-	-	-	0.31	0.30	-	-	-
	24%	19%	21%	-	-	-	5%	9%	-	-	-
121	0.27	0.23	-	-	-	-	0.29	0.32	-	-	-
	24%	5%	-	-	-	-	13%	24%	-	-	-
140	0.34	0.28	-	-	-	-	0.31	0.30	-	-	-
	67%	38%	-	-	-	-	50%	43%	-	-	-

6.2 Investigation of 3D effects

It was also necessary to determine if there were any three-dimensional effects on the models, due to their finite span. One way this was verified was by instrumenting the flat plate model with 4 additional spanwise thermocouples, all at a steamwise distance of 110 mm from the leading edge. The model was also modified to accept extender plates which doubled the span of the model from 2.5 inches to 5 inches. If the data from the thermocouples without the extenders matched the data with the extenders it would indicate that there were no significant three dimensional effects. The data with and without the extenders is presented in Figure 34.

At the edges of the model it is obvious that there is a significant three-dimensional effect due to the differences between the two cases. At the thermocouples near the center there is very little variation between the two cases. This seems to indicate that near the centerline the flow over the model can be assumed to be essentially two dimensional, and free from any edge effects. While this indicated that the data along the centerline of the flat plate was not affected by the span of the model, it was not clear if this result would apply to the curved ramps as well. To investigate three dimensional effects on the curved ramps, untripped PSP data over the Curved 16 model were analyzed for spanwise pressure gradients. Spanwise pressure data were extracted at increasingly large streamwise distances from the leading edge. If there was a significant change in pressure in the spanwise direction it would indicate that there were three dimensional effects. Figure 35 shows these data. It is evident from this plot that there is almost no spanwise variation in pressure (other than noise) at any point along the model curvature.

This issue arose again when collecting data over the Curved16 model. This model was instrumented with both off-center and centerline thermocouples, and after taking data it

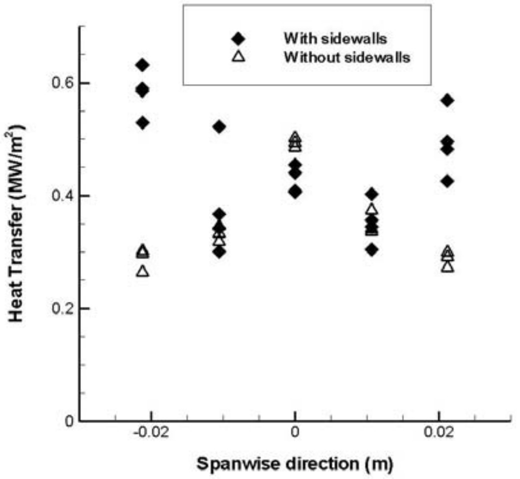

Figure 34: Heat flux data taken with and without model extender plates. Centerline corresponds to y=0.

was noticed that there was a distinct “step” behavior in the heat transfer data, resulting from the off-center thermocouples reading higher than expected. Figure 36 shows the data from the centerline and off-center data. It is unclear what is causing this since all other indicators show no three-dimensionality. Also, this same effect is not seen in the Linear10 data which also was fitted with off-center thermocouples. This issue is still unresolved, and the rest of the data presented here for the Curved16 model are only from centerline gages.

7 Laminar and tripped boundary layers over a baseline flat plate model

After the gages were verified and the effect of three-dimensionality had been investigated, the study concentrated on obtaining comparative measurements between the models in the Air-4 condition [54, 55]. The flat plate was chosen as the baseline for this comparison as it was a relatively simple flow field with the available analytical solutions already discussed. A plot of the heat transfer data compared to the PSP image of the flat plate with no protuberances installed can be seen in Figure 37. These data shows reasonably good agreement between the theoretical heat transfer from Simeonides. Also, it can been seen that the pressure distribution over the model is roughly constant (small fluctuations in the data are most likely just noise). While this is qualitatively what we would expect, we also wanted to investigate the quantitative levels to see if they matched theory and data measured with a static pressure gage. This was accomplished by comparing the PSP levels to an Endevco pressure transducer mounted in the plate as well as the perfect gas prediction. Table 5 shows the comparison between these values. There is very good agreement between the Endevco gage measurements and the perfect gas prediction. The PSP data and the predictions and Endevco data disagree by a factor of up to three. This indicates that there are issues either

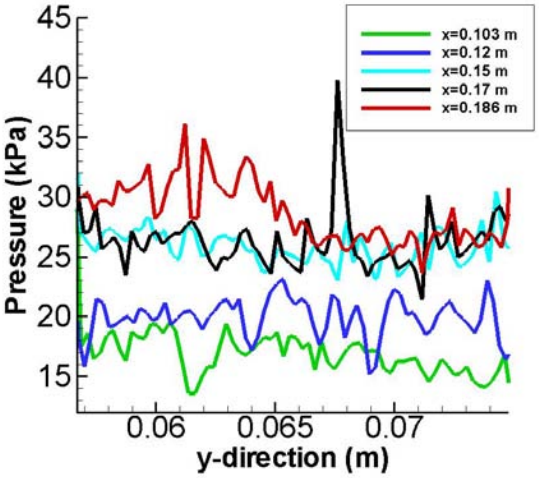

Figure 35: Spanwise pressure data on Curved16. Centerline corresponds to y=0.

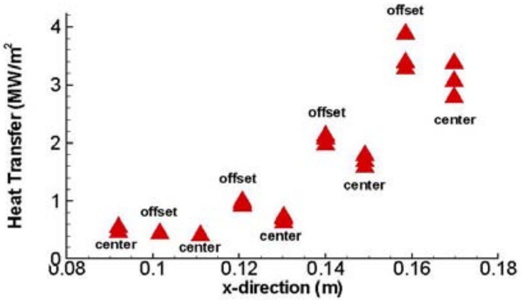

Figure 36: Curved16 heat transfer data including off-center thermocouples. Indicated offset thermocouples measure a higher than expected heat flux.

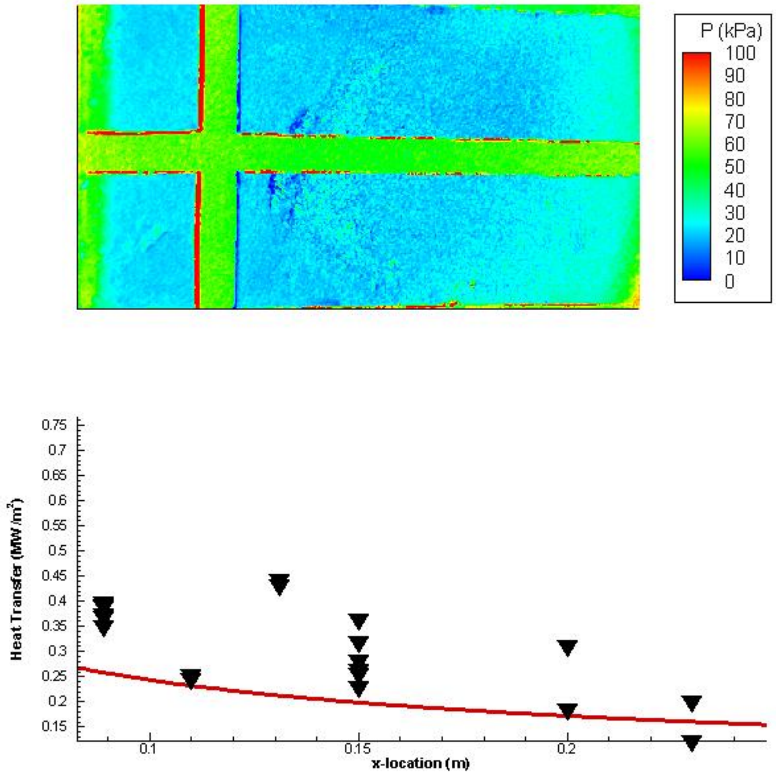

Figure 37: Untripped flat plate PSP data (top) and the corresponding heat transfer (bottom). The solid line is the prediction from Simeonides. PSP data were not collected along the two orthogonal strips (shown in green) due to the presence of thermocouples.

with the method of calibration, or with the radiometric method of data collection for the PSP. Since the calibration method has been used in other facilities with success it is most likely that the use of the radiometric method should first be investigated.

Next, data were taken over the flat plate with the diamond tripping elements installed. The data were compared against the Van Driest II turbulent heat flux prediction [50]. The heat transfer and PSP data with the diamond roughness elements installed can be seen in Figure 38.

These data indicate that the post-trip heat transfer levels agree best with the Van Driest II prediction. This does not provide conclusive proof that the boundary layer has transitioned, only that the vortices formed from the tripping elements cause a heat flux augmentation on the order of the turbulent heat flux augmentation.

Table 5: Comparison of Endevco gage data, perfect gas prediction, and PSP data at gage location

Configuration	Perfect Gas (kPa)	Endevco (kPa)	PSP (kPa)
No tripping element	8.13	8.40±0.84	20.68
With tripping element	-	9.12±0.91	18.36

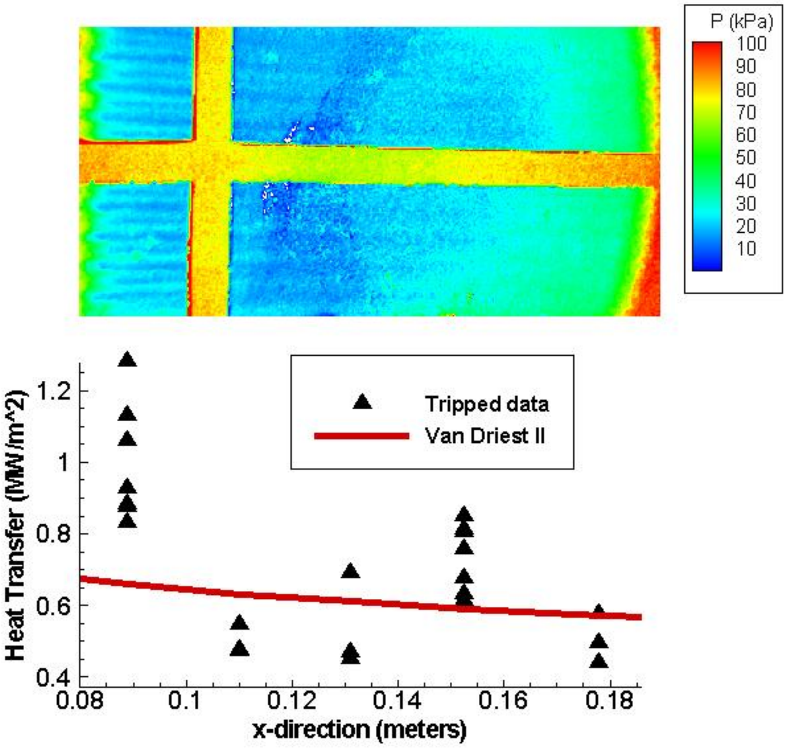

Figure 38: Tripped flat plate heat transfer and the corresponding PSP data

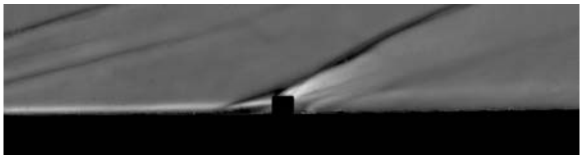

Figure 39: Schlieren image of the flat plate model with diamond tripping element installed in Air-4 (flow from left to right)

The vortices generated by the roughness elements can be seen forming directly behind the trip in the PSP image. Visual inspection seems to indicate that the vortices dissipate downstream of the trip, and cross sectional pressure distributions from the PSP confirm this. Whether or not these vortices breakdown into turbulence or dissipate into a laminar boundary layer is not clear. Based on these current diagnostic capabilities we were unable to definitively determine if transition occurs on the model. Due to the relatively low Reynolds number and short model length it is believed to be unlikely that transition occurred and that the augmented heat flux was due to the effects of the roughness generated vortices.

As a further illustration of the flow after the tripping elements, Figure 39 shows a Schlieren image of the flat plate with the diamond tripping element installed during a shot. The upstream seperation shock, expansion fan, and reattachment shock can all be seen in the image. While this image does show the shock structure formed around the tripping element nicely it does not give any conclusive evidence about the state of the boundary layer after the trip.

An additional comparative study was run looking into the effects of roughness geometry on the vortices. This was done using the three different roughness element geometries discussed in Section 4. The main goal of this portion of the study was to determine the effect of roughness geometry on the distance the vortices would be maintained downstream before they broke down. In order to accomplish this, a quantitative method of determining the vortex breakdown length was required. The method that was developed involved turning the gray scale PSP image into two binary images. The thresholding level was chosen so that on one end it was one step below the vortices being completely blacked out, and on the other end it was one step above the vortices being completely whited out. This threshold level was different for each geometry due to the difference in the strength of the vortices generated by the protuberances. These two images were used to set a left and right confidence bound on the location where the vortices dissipated. On each image, two bounds (shown as vertical dashed lines) on the last observable location of the individual vortices are marked. This is determined to be the region of vortex breakdown. Figures 40, 41, 42, and 43 show the breakdown behind the diamond protuberances, and triangle protuberances 2a, 2b, and 2c respectively. Additionally, spanwise pressure distributions are plotted for the three different trip geometries in Figures 44, 45, and 46. These indicate that each trip is generating different vortex structures behind the protuberance elements. Trip 2a has the most disorganized vortex structure. Trips 2b and 2c have similar structures though the fluctuations are stronger for Trip 2c. These results are in contrast with Berry [43] who found no organized vortex structures with these trip designs in either laminar or turbulent regions.

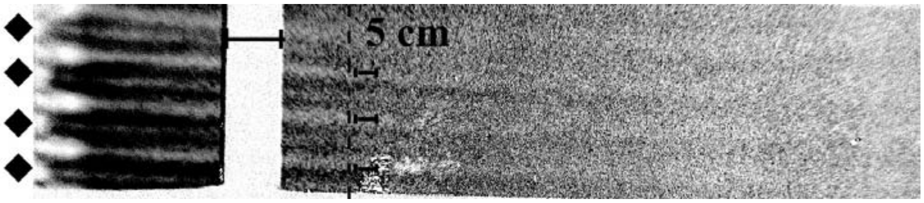

Figure 40: Vortex breakdown behind diamond roughness

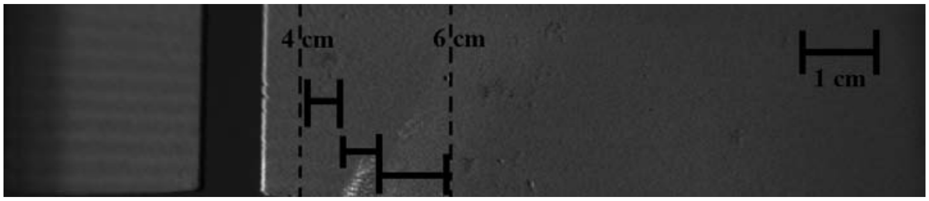

Figure 41: Vortex breakdown behind triangle protuberance 2a

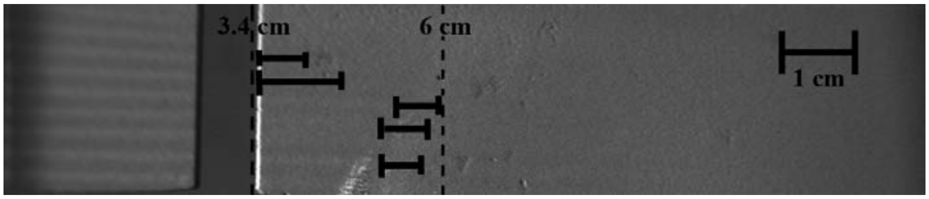
3.4 cm
6 cm
1 cm

Figure 42: Vortex breakdown behind triangle protuberance 2b

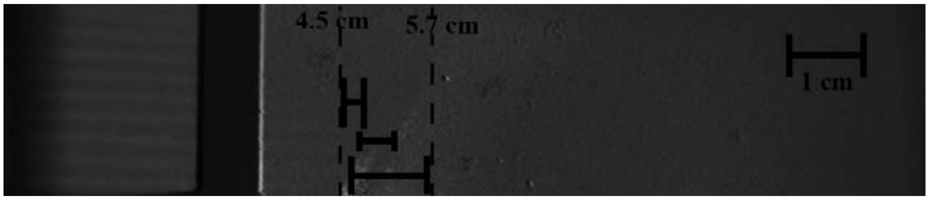
4.5 cm
5.7 cm
1 cm

Figure 43: Vortex breakdown behind triangle protuberance 2c

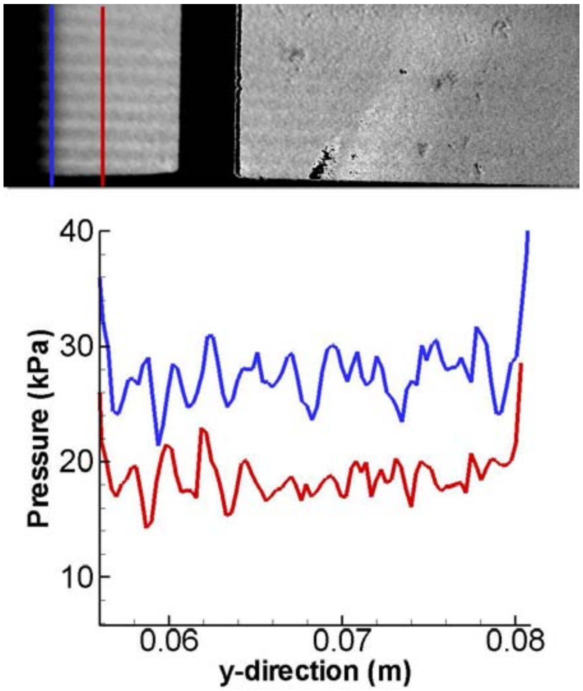

Figure 44: Spanwise pressure distribution for Trip2a on flat plate

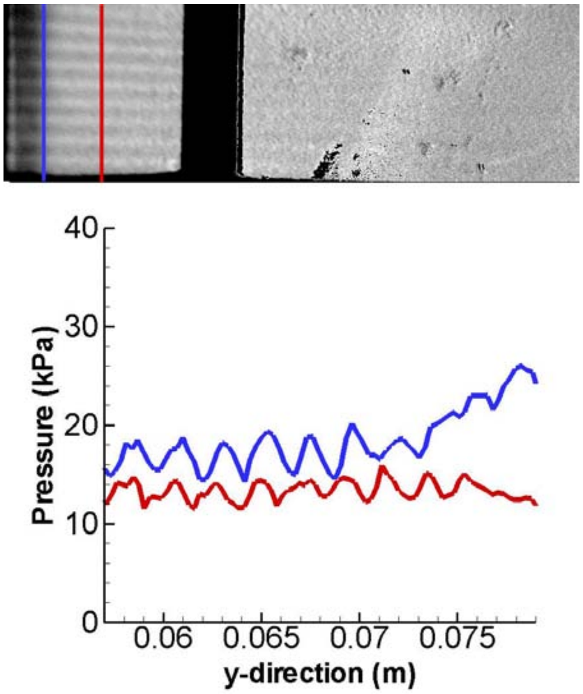

Figure 45: Spanwise pressure distribution for Trip2b on flat plate

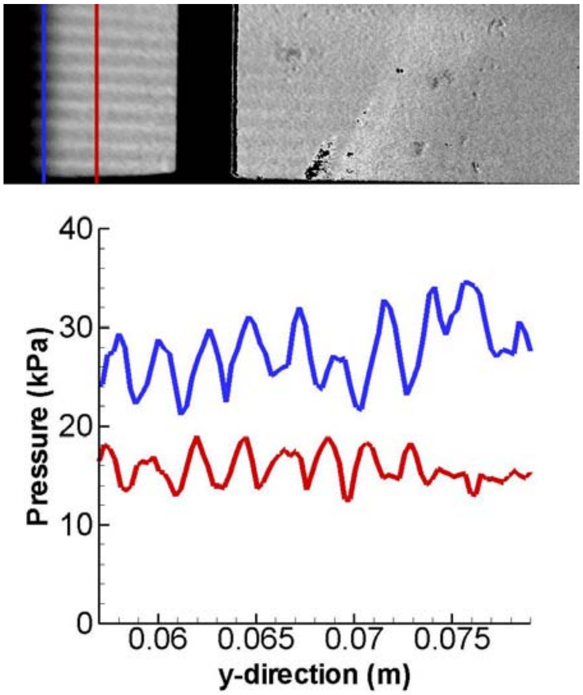

Figure 46: Spanwise pressure distribution for Trip2c on flat plate

8 Laminar and tripped boundary layers over linear and curved compression ramp models

The first compression ramp model to be tested was the Linear10 model, in both tripped and un-tripped configurations. Figure 47 shows the comparison between the heat transfer data and the PSP data over the Linear10 model in the untripped configuration.

The untripped heat transfer for this model is best fit by a linear increase after the start of the ramp. The comparison between the tripped heat transfer and PSP data for the Linear10 model is shown in Figure 48.

The structure of the vortices generated by the roughness elements for this model is significantly different than in the flat plate case, and this is reflected in both the heat transfer and the PSP data. The heat transfer data show three distinct zones. The transition between the first and second zone can be seen to correspond well with the location of vortex breakdown on the PSP image. The location of the transition to the third zone has no apparent associated feature on the PSP image, and the cause is unclear. The PSP image shows that the vortices have significant curvature towards the edge of the model, and seem to be sustained for a longer distance than those on the flat plate. It is useful here to compare the untripped data to the tripped data, Figure 49. This figure shows that the tripped data are higher than the untripped at the beginning, but that downstream on the model (by the sixth thermocouple station) it relaxes back to the untripped values. This indicates that, while the roughness elements do have a destabilizing effect on the boundary layer, this effect dissipates downstream of the roughness elements.

The untripped heat transfer over the Curved10 model is presented in Figure 50. A curve

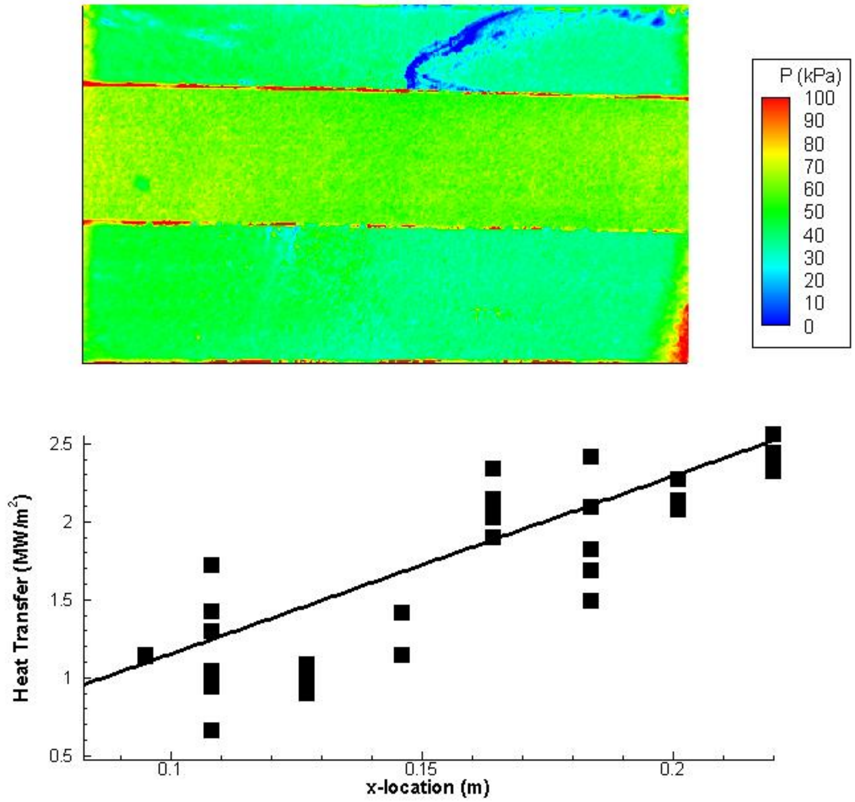

Figure 47: Comparison of untripped PSP data (top) and heat transfer (bottom) on Linear10 model. The solid line is the curve fit to the heat transfer data. PSP data were not collected along the middle strip in the image due to the presence of thermocouples.

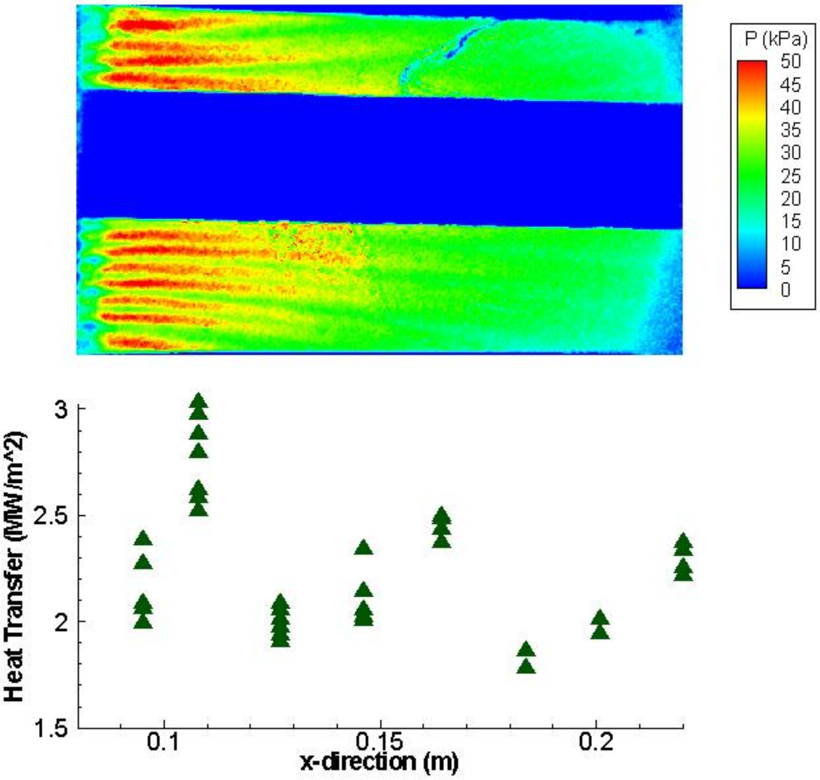

Figure 48: Comparison of tripped PSP data (top) and heat transfer (bottom) on Linear10 model

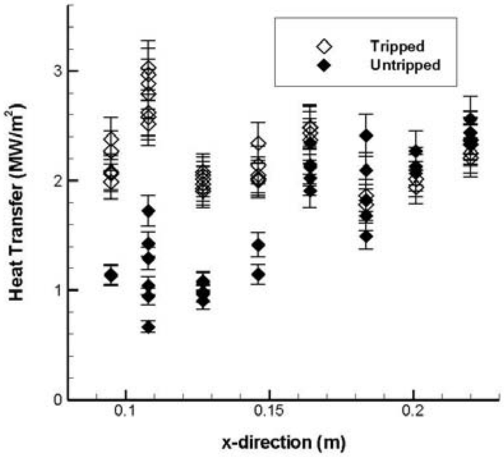

Figure 49: Comparison of tripped and untripped heat transfer data over Curved10

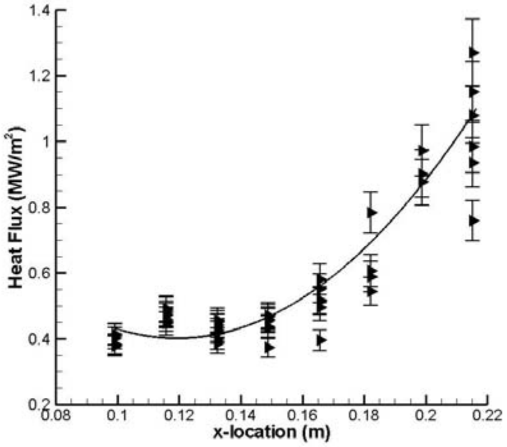

Figure 50: Untripped heat transfer data over Curved10 model

fit done to the laminar heat transfer data shows that it can be reasonably well described by a quadratic, given by Equation 16.

$$q = 74.27x^2 - 17.73x + 1.46 \tag{16}$$

If the surface if the model was to be described by an equation, it would also be described by a quadratic. Figure 51 shows the heat transfer over the Curved10 model with the diamond roughness elements installed.

To gain better insight into the effects of the roughness elements it is useful here to compare the untripped heat transfer to the tripped heat transfer for the Curved10 model, Figure 52. This plot shows that with the roughness elements installed the heat transfer is significantly higher at each x-location. This indicates that the vortices generated by the roughness elements has a significant destabilizing effect on the boundary layer forming

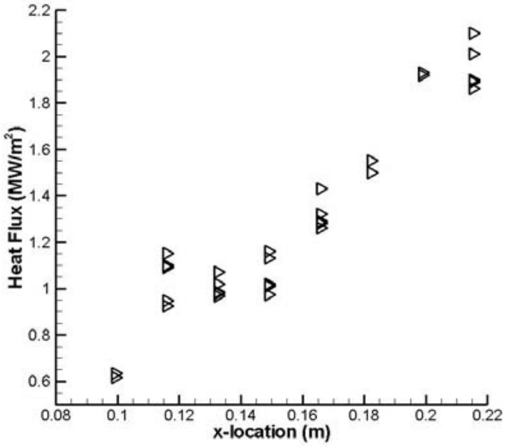

Figure 51: Tripped heat transfer distribution over Curved10 model

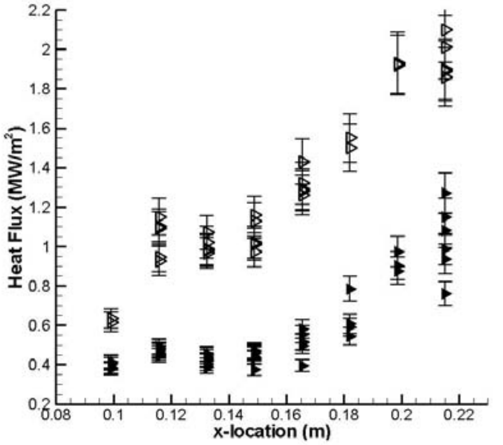

Figure 52: Comparison of tripped and untripped data over Curved10

over the model.

The untripped heat transfer and PSP data over the Curved16 model, are shown in Figure 53. A curve fit done to the laminar heat transfer data shows that it can be reasonably well described by a quadratic given by Equation 17. The surface equation of this model is also a quadratic function. The PSP data show a non-linear increase in pressure. A steamwise plot of the PSP pressure over Curved16 compared to the prediction given by the method of characteristics can be seen in Figure 54.

$$q = 915.8x^2 - 197.3x + 11 \tag{17}$$

Similar to the flat plate PSP data, the pressure levels do not match predictions. This further indicates that more work must be done before quantitative pressure levels from the PSP can be trusted.

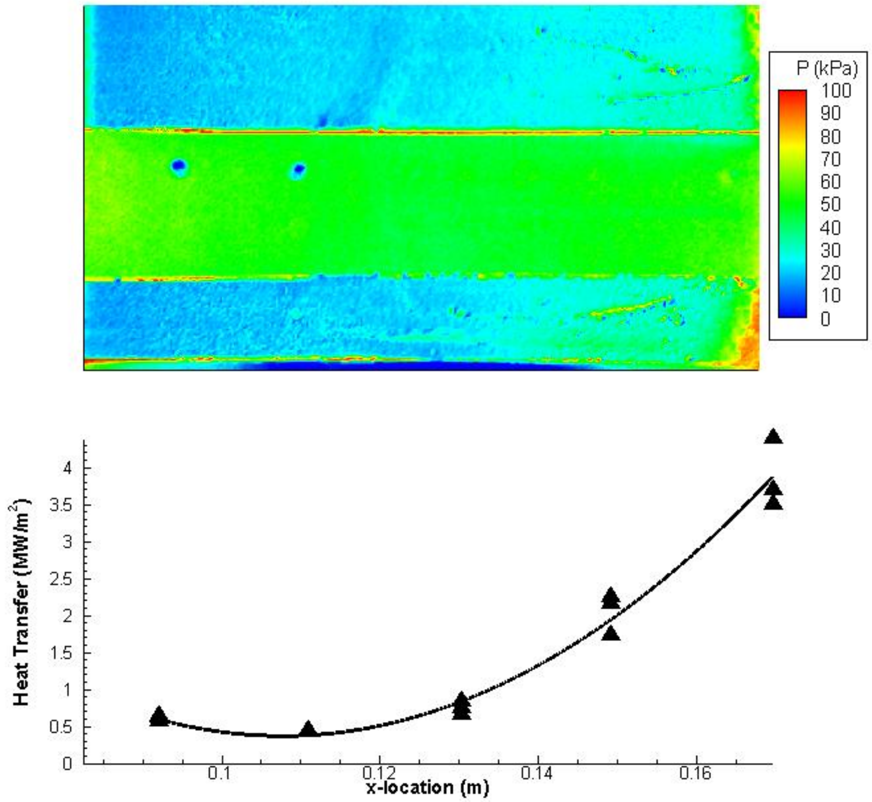

Figure 53: Untripped PSP (top) and heat transfer (bottom) data over Curved16. Solid line is a heat transfer data. The middle section of the model was left unpainted due to the presence of thermocouples

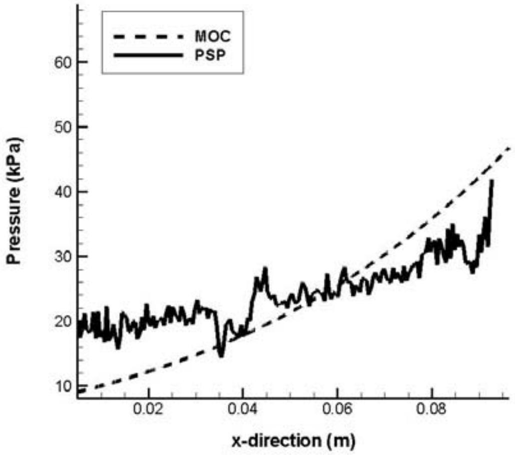

Figure 54: Surface PSP pressure data compared to method of characteristics prediction for the external flow over Curved16.

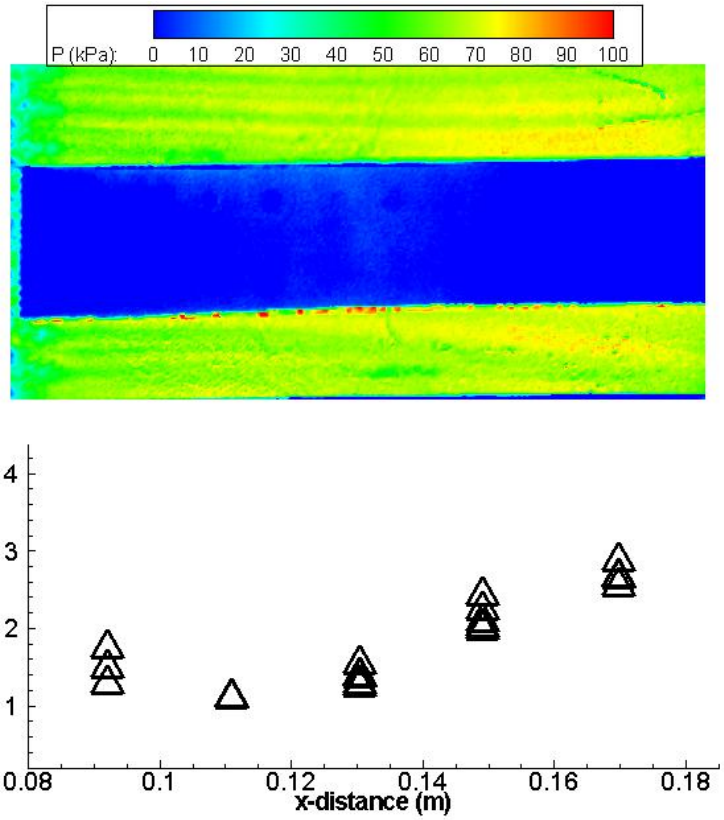

Figure 55: Tripped PSP (top) and heat transfer (bottom) data over Curved16.

The tripped heat transfer distribution compared to the PSP data for Curved16 can be seen in Figure 55. The same vortex structure that was seen in both the flat plate and Linear10 cases is seen here, but in this case the vortices are maintained much further down the ramp. Thus, the surface curvature appears to have some sort of stabilizing effect on the vortices. Towards the end of the ramp the curvature vortices causes them to move to the edge of the model. It is possible that this three dimensional effect is responsible for the relaxation in the heat flux seen over this model. Unfortunately, data were not obtained along the centerline of the model (where the thermocouples were located) so it was impossible to conclusively determine if this was the case. Again we can compare the heat transfer distribution in the tripped and untripped case for this model, Figure 56.

For the first three thermocouple locations the tripped data are higher than the untripped data, which is to be expected. At the second to last location the data fall over each other almost exactly, and at the last location the untripped heat flux actually measures higher than the tripped heat flux. This indicates that the vortices are most likely dissipating and the boundary layer is in the tripped case is returning to a laminar state. Figure 57 shows the untripped heat transfer distribution over the Curved25 model. This data are reasonably well described by a quadratic, given by Equation 18. The surface equation of this model can also be described with a quadratic equation.

$$q = 1029x^2 - 239.6x + 14.37 \tag{18}$$

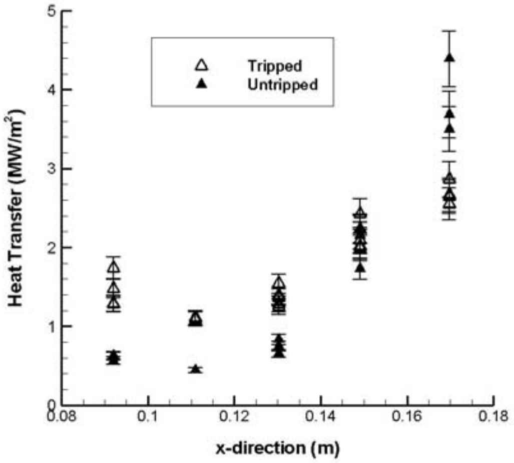

Figure 56: Comparison of tripped and untripped heat transfer for Curved16

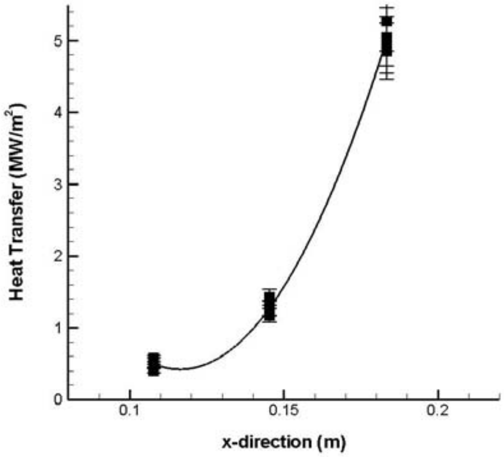

Figure 57: Untripped heat transfer distribution over Curved25

The tripped heat transfer for Curved25 can be seen in Figure 58. Again for this model, at the first two thermocouple locations the measured heat flux is higher in the tripped case than in the untripped case. At the last thermocouple location the untripped heat flux is higher than in the tripped case. Similar to the Curved16 and Linear10 cases, this seems to indicate some sort of relaxation of the disturbances in the boundary layer over the model, or possibly three dimensional effects caused by the induced vortices.

The untripped data over the Cubic1 model is presented in Figure 59. When fitting a curve to the untripped Cubic1 data, as was done in the other compression ramp cases, it is unclear whether it is best described by a cubic or quartic fit, given by the following two equations:

$$q = -2743x^3 + 1726x^2 - 285.7x + 14.67 \tag{19}$$

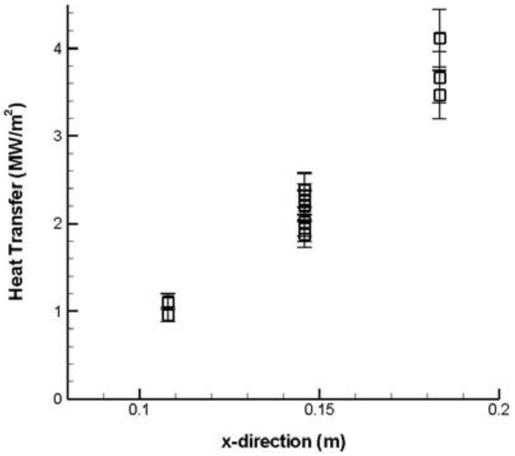

Figure 58: Tripped heat transfer data over Curved25

$$q = 56550x^4 - 38650x^3 + 10070x^2 - 1125x + 45.48 \tag{20}$$

This indicates that as the surface equation of the model becomes more complex so does the trend in the heat flux.

The tripped data over Cubic1 are seen in Figure 60, and the comparison between the tripped and untripped Cubic1 data can be seen in Figure 61. This data shows a similar trend as the Curved25, Curved16, and Linear 10 models, only in this case, by the sixth thermocouple, the untripped data actually are higher than the tripped value. This supports the idea that the vortices are promoting a significant three-dimensional effects over the model which effect the heat transfer distribution. This also seems to indicate that the smaller the radius of curvature is, the stronger the relaxation. Since no PSP data were obtained over this model it is unclear what the development of the vortices looks like as they progress down the ramp.

9 Laminar boundary layers: The effect of wall geometry

While the previous sections reported on the results obtained over each individual model, it is useful to compare the results between models in order to gain more insight into the results. The first comparison that can be made is between the untripped heat transfer from the Linear10 model and the Curved10 model, Figure 62.

At each location the heat flux on the Linear10 model is higher than on the Curved10 model. This is interesting as the flow undergoes the same final turning angle in each case. This indicates that even though the surface curvature will cause boundary layer distortions it still does not have as drastic an effect on the boundary layer as the shock generated at the compression corner.

As has been mentioned previously in this report, the results seem to indicate that the trend in heat flux has the same form as the surface equation of the model. This is best

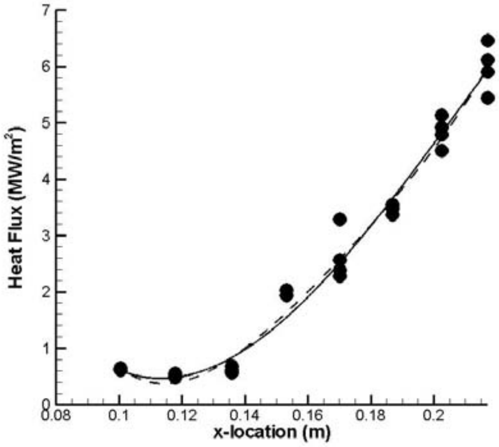

Figure 59: Untripped heat transfer data over Cubic1

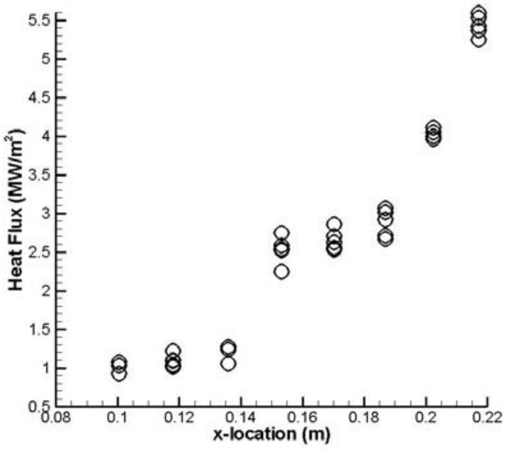

Figure 60: Tripped heat transfer data over Cubic1

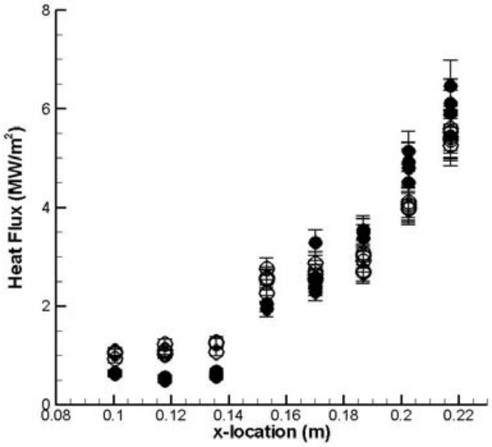

Figure 61: Comparison of tripped and untripped heat transfer data over Cubic1

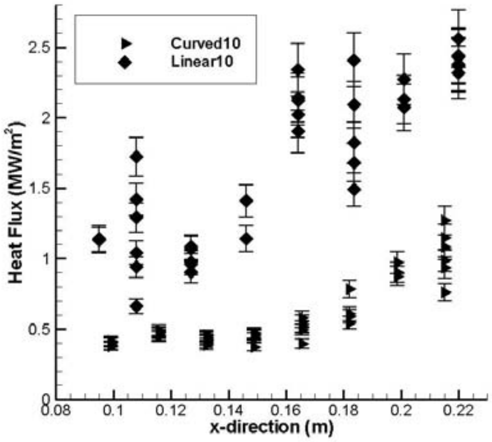

Figure 62: Comparison of untripped Linear10 and Curved10 heat transfer distributions

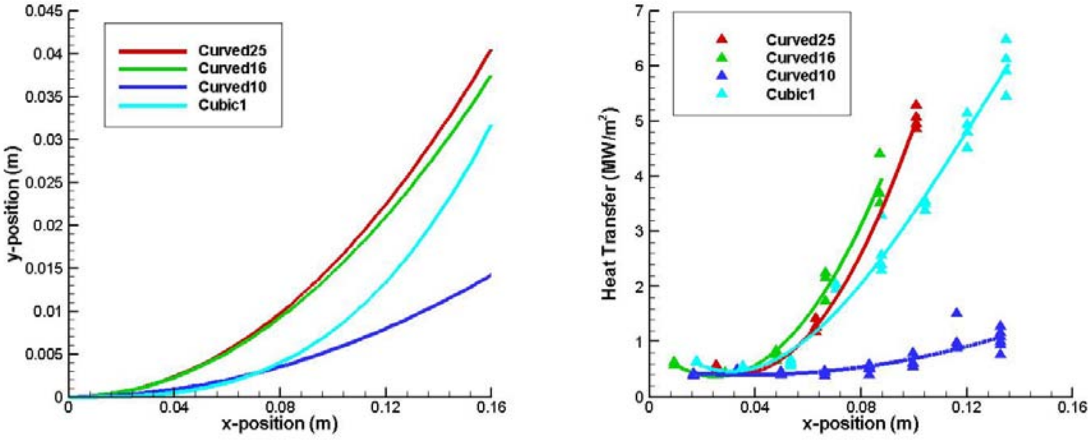

(a) (b)

Figure 63: (a) Model surface equations (b) Experimental heat transfer measurements and curve fits

illustrated in Figure 63. This figure shows a comparison between the experimental heat transfer levels of all the curved compression models and their associated surface equations. The two plots compare rather well, and support the assertion that there is a strong link between the surface equation and the heat transfer.

Another interesting comparison that can be made is between the Curved25, Curved16, and Linear10 models. So far the data presented for Curved16 has been for the curved portion of the model only and did not include the final linear part of the ramp. A plot of the data from the three models, including the data Curved16 after the curvature, is shown in Figure 64. It is obvious that soon after the section of curvature the heat flux on Curved16 relaxes back to the levels near those measured by Linear10, and then begins increasing in a linear fashion. This is another strong indicator that the heat transfer levels are directly linked to the surface geometry of the model.

After gathering these data it was decided to look into the literature and see if this trend could be observed in previous studies which looked at curved compression ramps. Two other studies were found whose data could be analyzed to see if they showed the same link between surface curvature and heat transfer distribution. Mohammadian [56] took experimental data over a cubic compression surface for use in comparison with a numerical solution he had developed based on the method of Chang [57]. Figure 65 shows the results of the experimental study, with the curve fit which best describes the data, compared to the data from the Curved16 and Cubic1 models.

The function for the curve fit is given by a forth quartic polynomial given in Equation 21. This is interesting since it was unclear if the data collected over Cubic1 was better described by a cubic fit or a quartic fit. This seems to support the idea that as the surface geometry of the model becomes more complex so does the heat transfer increase.

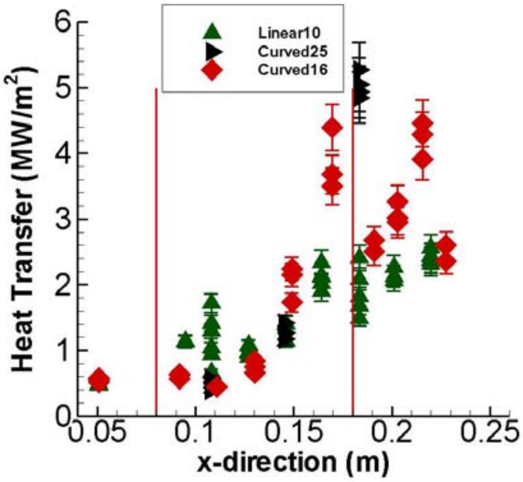

Figure 64: Comparison of Curved16, Curved25, and Linear10. Vertical lines indicate the beginning and ending of curvature on the Curved16 model

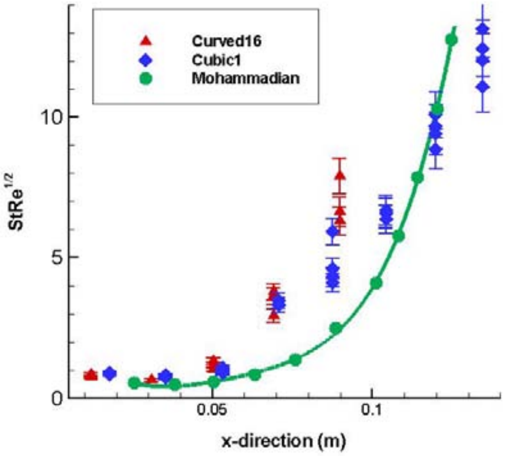

Figure 65: Comparison of Curved16 and Cubic1 data with Mohammadian data. Solid line is quartic fit to Mohammadian data

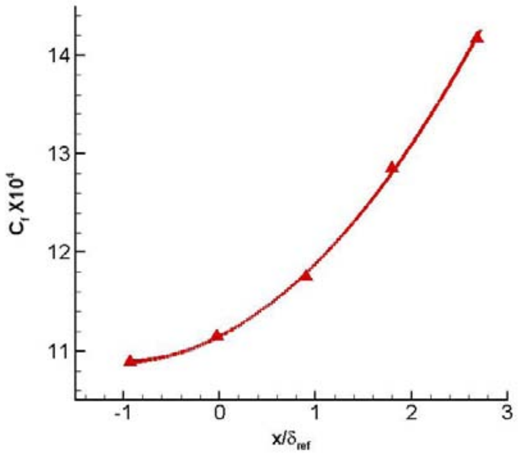

Figure 66: Skin friction data from Donovan *et al.* [9]

$$q = 0.1514x^4 - 1.301x^3 + 4.404x^2 - 6.33x + 3.642 \tag{21}$$

The study by Donovan *et al.* [9], which served as the basis for the design of the Curved16 model, also provided some experimental data which could be analyzed. In this study they measured the skin friction over a model with a quadratic surface geometry. This should be directly relatable to heat transfer if we assume that the Reynolds analogy is correct. The Reynolds analogy says that there is a linear relationship between skin friction and heat transfer. While the accuracy of this method has been questioned by some it is a reasonable assumption for comparisons sake. Figure 66 shows the skin friction data that was collected by Donovan *et al.*, and the best curve fit to the data.

The curve fit to these data is given by the quadratic function in Equation 22. If we assume that the Reynolds analogy holds then this means that the heat transfer would also have a quadratic increase. This seems to indicate that the trend of heat flux having the same form as surface geometry holds between different facilities as well as models.

$$q = 0.2365x^2 + 0.4978x + 11.15 \tag{22}$$

10 Theoretical predictions of heat transfer over compression ramp models

Since the early 1950's there have been many attempts to predict the flow characteristics in the presence of heat transfer and an adverse pressure gradient. The goal of these studies was to simplify the Navier-Stokes equations including terms to account for a non-linear adverse pressure gradient. This problem is especially difficult because it does not easily lend itself to a similarity solution. Most of these studies assume profiles for different quantities through the boundary layer (such as temperature, normal and axial velocity, etc), and then solve the equations using an integral method.

Beckwith [58] developed a method for arbitrary Prandtl number (assumed to be near unity), and arbitrary wall pressure and temperature distributions. The limiting assumptions here were that the velocity and thermal boundary layer thicknesses were equal, and that viscosity varied linearly with temperature. A 5th-order polynomial was used to approximate the normal temperature change through the boundary layer. Good agreement was found for flat plate and cylinder geometries when compared to other solution methods that were known to be accurate. No comparison was made with experimental data.

Morduchow and Grape [59] also developed a numerical technique for this problem. Their limiting assumptions included a Prandtl number of unity and a linear relationship between temperature and viscosity. They utilized a 6th-degree velocity profile and a 7th-degree stagnation enthalpy (and therefore temperature) profile. In addition to being able to predict heat transfer and skin friction, the code they developed had the ability to predict the point of separation in an adverse pressure gradient flow. The studies main concern was to numerically investigate the effect that wall temperature and pressure gradient had on the skin friction and heat transfer over the surface. They found that the effect of changing the wall temperature affected the skin friction and heat transfer through the pressure gradient and viscosity terms. Overall, cooling the wall in the presence of an adverse pressure gradient was found to increase both quantities, while heating the wall had the opposite effect. Also, as the ratio of the wall temperature to the freestream temperature decreased the heat transfer was found to increase. Also, cooling of the wall in an adverse pressure gradient served to delay separation. The authors also claimed that they had created an accurate method to predict separation, but did not compare their predictions with any experimental data.

Cheng, *et al.* [57] developed a method for prediction of boundary layer quantities in the presence of a pressure gradient created by a blunt nose on a flat plate at an angle of attack. In order to do this they broke the flow into three distinct regions: the boundary layer, the detached shock layer, and the entropy layer which lies between the first two. Under these conditions they applied a small perturbation procedure which yielded a similarity solution to leading order. The entropy layer was described by a pressure-area relation, and the detached shock layer inviscid shock-layer theory was used. The limiting assumptions here are that the specific heat ratio is one and that there is a strong bow shock. The results from this method showed reasonable agreement with both previous theories as well as experimental heat transfer and Schlieren data. The results here were extended by both Stollery [60] and Mohammadian [56]. They were able to extend the previous method to curved compression surfaces and other geometries with non-linear pressure gradients. One of the major modifications these studies had to make was to change the pressure law used to determine the pressure gradient. Cheng, *et al.* used a Newton-Busemann approximation for the pressure gradient. When this was applied to non-linear pressure gradients it resulted in unstable oscillatory solutions. It was found that by replacing this approximation to one without the Busemann term, or with the tangent-wedge approximation, these oscillations could be eliminated from the solution. Stollery was able to reproduce major flow features seen in experimental data with his method, though he mentions that if the boundary layer is strongly non-similar or approaching separation this method will breakdown. Mohammadian found that the modified Cheng analysis with the tangent-wedge pressure approximation could adequately predict boundary layer growth over a cubic model, but had much poorer agreement to the experimental heat transfer over the model. He concluded that this was most likely due to the similarity assumption inherent in the model which was failing in the presence of the highly non-similar boundary layer over the ramp.

Holden also performed a theoretical and experimental study of the characteristics of curved compression surfaces. His theoretical study began with the Navier-Stokes equations in curvilinear coordinates, and his analysis included the effects of pressure fluctuations in the direction normal to the boundary layer. This is a feature that most approximate theories do not include, but one that is known to be important on highly non-similar boundary layers over curved surfaces. Holden uses both the Stewatson-Illingsworth transformation, as well as assumed profiles for the velocity and enthalpy in order to find a system of differential equations which can be solved. He was able to obtain reasonably good agreement with experimental results over curved surfaces.

Two studies also developed approximate solutions to the boundary layer equations in order to provide an easier way to predict quantities such as the boundary layer thickness and heat transfer over the curved ramp models. Both of these methods were applied to the experiments run in the HET in order to try to get theoretical data to compare the experimental results to. The first study was done by Cohen and Resotko [61]. They were able to develop a method to approximate boundary layer characteristics by applying the Stewartson transformation to the continuity equations. They were able to derive a set of dimensionless parameters which could be used to represent non-dimensional parameters in the flow. There parameters are the shear parameter, Equation 23, the correlation number, Equation 24, and the heat transfer parameter, Equation 25.

$$l = \frac{\theta}{u_e}\frac{T_w}{T_e}\left(\frac{\partial u}{\partial y}\right)_w \tag{23}$$

$$n = -\frac{u_{e_x}\theta^2}{v_w}\left(\frac{T_w}{T_e}\right)^2\left(\frac{T_0}{T_e}\right) \tag{24}$$

$$r = n\theta\frac{T_w}{T_e}\left[\frac{\partial}{\partial y}\left(\frac{T}{T_e}\right)\right]_w \tag{25}$$

The correlation parameter can be calculated directly using Equation 26.

$$\frac{n}{P'\frac{T_0}{T_e}} = A\left(\frac{T_e}{T_0}\right)^{-K} M_e^{1-B}\int_0^{\frac{x}{L}}\left(\frac{T_e}{T_0}\right)^K M_e^{B-1} d\left(\frac{x}{L}\right) \tag{26}$$

The left hand side of the equation is left as it is to facilitate later calculations. The coefficients A and B are tabulated based on boundary conditions of the particular flow being investigated. The integral term can be evaluated numerically since it is assumed that conditions at the edge of the boundary layer are known (in the case of the work in HET they were known from the MOC calculations). Once the correlation parameter is known, l can be determined based on tabulated values. It is also possible to find what the authors term the "Reynolds analogy parameter", $\left(\frac{C_f \mathrm{Re}_w}{Nu}\right)_{\mathrm{Pr}=1}$, which is also tabulated as a function of n. With these three values it is possible to calculate the heat transfer using Equations 27, and 28.

$$C_f\sqrt{\mathrm{Re}_w} = 2l\sqrt{\frac{\frac{x}{L}P'\frac{T_0}{T_e}}{n}} \tag{27}$$

$$\frac{Nu}{\sqrt{\mathrm{Re}_w}} = \frac{C_f\sqrt{\mathrm{Re}_w}}{\left(\frac{C_f \mathrm{Re}_w}{Nu}\right)_{\mathrm{Pr}=1}} \tag{28}$$

The second study which gave an analytical approximation of the heat flux was done by Bertram and Feller [62]. They created a method to calculate skin friction, heat transfer, and boundary layer thickness in the presence of a known power-law pressure distribution. It utilized similar solutions to the boundary layer equations based on the work of Li and Nagamatsu [63], who showed that the pressure gradient parameter from the Falkner-Skan solution can be extended to the compressible case if we assume the flow is isentropic and hypersonic at the boundary layer edge. This corrected pressure gradient parameter is given by Equation 29.

$$\beta = \frac{1-\gamma}{\gamma}\frac{n}{n+1} \tag{29}$$

Where, in this case, n is the exponent which describes the power law pressure distribution. Based on this parameter β and the ratio of wall to freestream enthalpy they were able to tabulate a series of parameters which could be used to calculate 4 coefficients, given by Equations 30, 31, 32, 33.

$$K_1 = f_w^{''}\frac{\sqrt{2\left(1+n\right)}}{0.664} \tag{30}$$

$$K_2 = \frac{f_w^{''}}{0.332\sqrt{2\left(1+n\right)}} \tag{31}$$

$$K_3 = -\frac{S_w^{'}}{S_w}\frac{\sqrt{2\left(1+n\right)}}{0.664} \tag{32}$$

$$K_4 = \frac{\frac{2}{\sqrt{2(1+n)}}\int_0^\infty \left(S+1-f'^2\right)d\eta}{\sqrt{2}\left[\int_0^\infty (S+1-f'^2)d\eta\right]_{\beta=0}} \tag{33}$$

Where the terms $f_w^{''}$, $S_w^{'}$, and the integral term in K_4 are tabulated as functions of the pressure gradient parameter β. Using these coefficients they were able to find equations for skin friction, heat transfer, and boundary layer thickness given by Equations 34, 35, 36, and 37.

$$\frac{C_f}{\overline{C_f}} = K_1\sqrt{\frac{p_w}{p_\infty}} \tag{34}$$

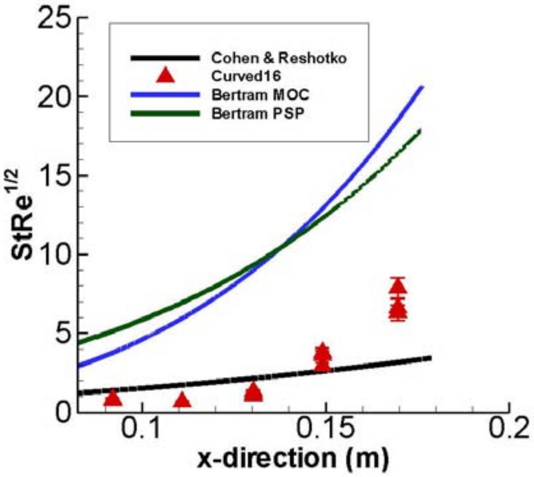

Figure 67: Theoretical model calculations carried out for conditions of the present study compared to Curved16 data

$$\frac{C_F}{\overline{\overline{C_F}}} = K_2\sqrt{\frac{p_{w,L}}{p_\infty}} \tag{35}$$

$$\frac{h}{\overline{\overline{h}}} = K_3\sqrt{\frac{p_w}{p_\infty}} \tag{36}$$

$$\frac{\delta}{\overline{\overline{\delta}}} = \frac{K_4}{\sqrt{\frac{p_w}{p_\infty}}} \tag{37}$$

Where h is the local heat transfer coefficient.

Both of these models were used to generate predictions for the Curved16 and Curved25 models. The results for the Curved16 model are shown in Figure 67. For the Bertram prediction, the pressure distribution from both the MOC calculations was used as well as from the PSP data.

It is obvious that neither of these models compares very well with the experimental data. The Bertram model, with both pressure distributions, is higher are every x-location than the experimental data. For the Cohen and Reshotko model it reads higher initially, and then intersects the experimental data at approximately 0.14 m. Figure 68 shows the results for the Curved25 model using only the MOC predictions of pressure.

This plot shows the same behavior as the Curved16 case with the Bertram model predicting consistently high, and the Cohen and Reshotko model starting high and then intersecting the data further downstream. At this time the reason for these errors is unknown. It is possible that since these methods are only approximations that they are not adequately modeling the flow investigated here. More work is being undertaken to understand these results better.

In addition to predicting the heat transfer, the Bertram model gives a method of calculating the expected boundary layer thickness. The predicted boundary layer thicknesses for the Curved25, Curved16, and Cubic1 models can be seen in Figure 69.

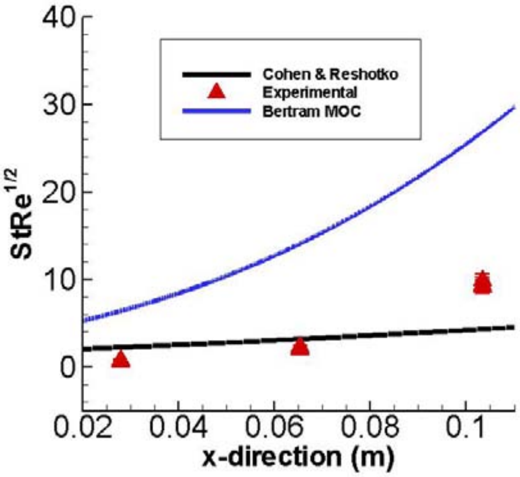

Figure 68: Theoretical model calculations for conditions of the present study compared to Curved25 data

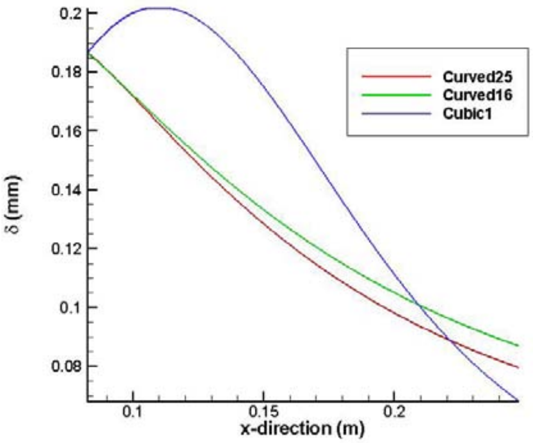

Figure 69: Theoretical boundary layer thicknesses calculated at the conditions of the present study

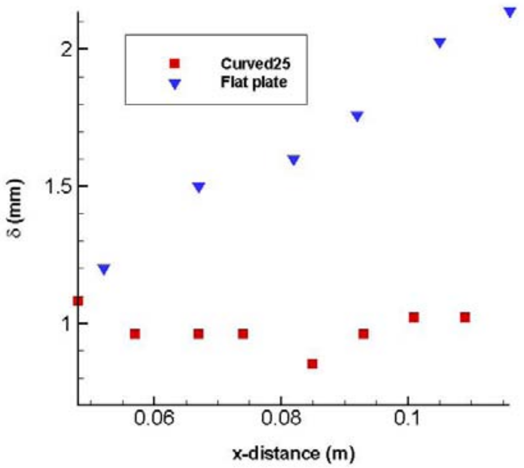

Figure 70: Boundary layer thicknesses measured from Schlieren images

One interesting feature from this plot is the inflection point in the boundary layer on the Cubic1 model. At the beginning of curvature the boundary layer grows, then further down the model there is an inflection point. This is due to the fact that the curvature is not constant on this model, and may explain why the heat transfer data on this model initially decreases before increasing sharply. Schlieren images were also taken of both the flat plate and the Curved25 model, and the boundary layer thickness was measured from these images. Figure 70 shows these two measured boundary layer thicknesses.

These measurements show that the boundary layer on the flat plate is growing as expected, and that the boundary layer on the Curved25 model is slightly decreasing. While the magnitude of the boundary layer thicknesses do not agree with the theory, they do follow the same trends.

11 The evolution of imposed vortex structures

Significant differences were observed in the imposed vortex structure evolution over models with different surface geometries. The diamond trip was installed in the flat plate, Linear10, and Curved16 models. The overall PSP images for these cases was already presented in the preceding section, but here it will be analyzed to determine the location of vortex break down in order to quantify the effects of surface geometry on the vortices. The same thresholding method used to analyze the flat plate images is used here. Figures 71, 72, 73 show the results.

The overall result shows that the effect of an adverse pressure gradient is to cause the vortices to survive longer downstream from the tripping element. On the flat plate the vortices begin dissipating at around 5 cm behind the tripping elements, while on the Linear10 model they survive till almost 11 cm and on Curved16 the survive to around 9.5 cm. Another interesting feature to note is the difference in structure between the vortices on the Linear10 and Curved16 models. The vortices formed near the edges of the Linear10 model seem to have significantly more curvature, terminating at the edge of the model rather than

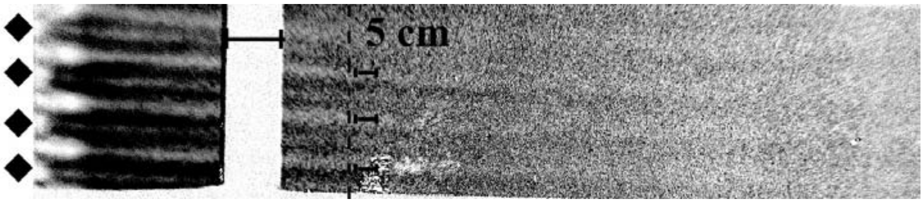

Figure 71: Vortex breakdown on flat plate

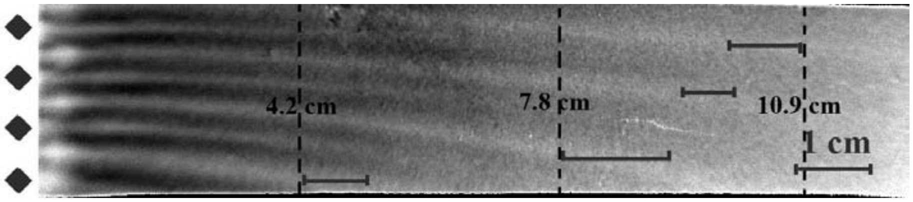

Figure 72: Vortex breakdown on Linear10

dissipating downstream. For the Curved16 model, the edge vortices still exhibit curvature towards the model edge, but not as much as the Linear10 case, and the edge vortices dissipate rather than terminating on the edge of the model. This is an important results as it indicates that the behavior of vortices are strongly affected by the wall curvature, and it seems to be a stabilizing influence. Additionally, pressure cross sections from the Curved16 model reveal that when the trips are installed significant three-dimensional effects exists on the model that is not observed in the untripped case. Figure 74 illustrates this by showing cross-sections of pressure at selected downstream locations (x=0.101 to 0.18 m). In the untripped case, no significant spanwise variation is observed at any downstream location. In contrast, by x=0.18m a significant (Δp=10kPa) pressure decrease is observed from the centerline to the edge of the model, which is consistent with the movement of the vortices on the model surface. The behavior and maintenance of the vortices thus appears to be linked to changes in the mean flow. Figure 75 shows where the pressure cross sections were taken along the ramp for both cases. The colors for the pressure cross sections correspond the the colored lines on the PSP images.

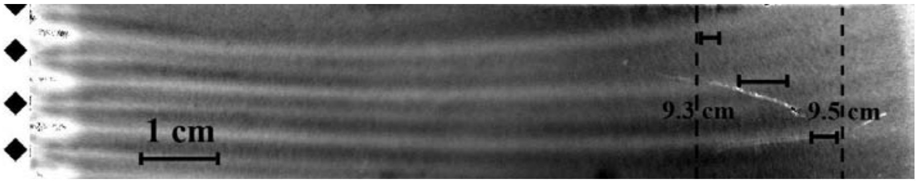

Figure 73: Vortex breakdown on Curved16

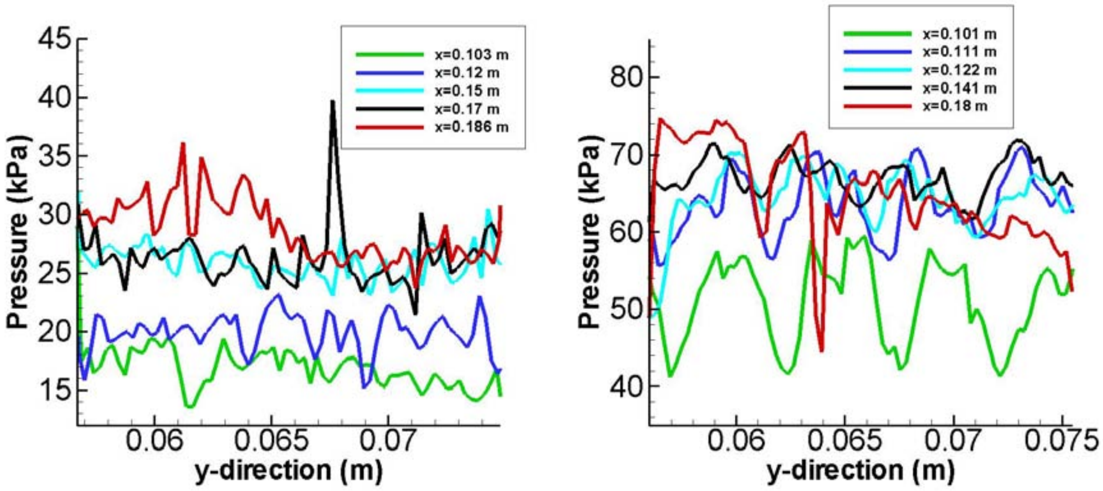

(a) (b)

Figure 74: (a) Untripped Curved16 pressure distributions (b) Tripped Curved16 pressure distributions. Y is in the spanwise direction with y=0 corresponding to the center of the model.

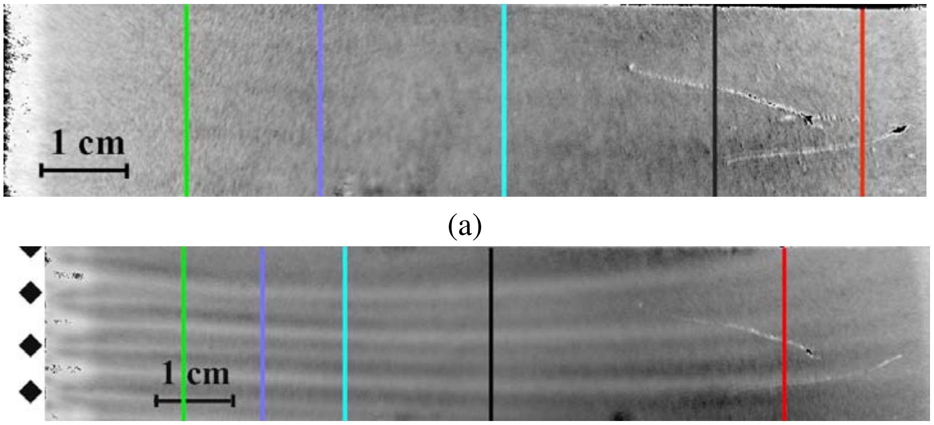

(b)

Figure 75: Curved16 PSP images with pressure cross-section locations marked for untripped (a) and tripped (b)

References

[1] S. Molder and E.J. Szpiro. Busemann inlet for hypersonic speeds. *Journal of Spacecraft and Rockets*, 3(8):1172–1176, 1966.

[2] F.S. Billig and A.P. Kothari. Streamline tracing: Technique for designing hypersonic vehicles. *Journal of Propulsion and Power*, 16(3):465–471, 2000.

[3] P. Bradshaw. Compressible turbulent shear layers. *Annual Review of Fluid Mechanics*, 9:33–54, 1977.

[4] E. F. Spina, A. J. Smits, and S. K. Robinson. The physics of supersonic turbulent boundary layers. *Annual Review of Fluid Mechanics*, 26:287–319, 1994.

[5] A. J. Smits and J. P. Dussauge. *Turbulent shear layers in supersonic flow*. Springer NY, 2006.

[6] A. Favre. *The mechanics of turbulence*. Gordon and Breach, 1964.

[7] C. Y. Wen and H. G. Hornung. Nonequilibrium dissociating flow over spheres. *Journal of Fluid Mechanics*, 299:389–405, 1995.

[8] P. A. Gnoffo. Planetary-entry gas dynamics. *Annual Review of Fluid Mechanics*, 31:459–494, 1999.

[9] J. F. Donovan, E. F. Spina, and A. J. Smits. The structure of a supersonic boundary layer subject to concave wall curvature. *Journal of Fluid Mechanics*, 259:1–24, January 1994.

[10] E. M. Fernando and A. J. Smits. A supersonic turbulent boundary layer in an adverse pressure gradient. *Journal of Fluid Mechanics*, 211:285–307, 1990.

[11] H. Goertler. On the three-dimensional instability of laminar boundary layers on concave walls. Technical Memo 1375, NACA, 1954.

[12] I. E. Beckwith and B. B. Holley. TP 1869, NASA, 1955.

[13] I. E. Beckwith, T. R. Creel F. J. Chen, and J. M. Kendall. Free stream noise and transition measurements in a Mach 3.5 pilot quiet tunnel. *AIAA paper*, (0042), 1983.

[14] L. de Luca, G. Cardone, D.A. de la Chevalerie, and A. Fonteneau. Goertler instability of a hypersonic boundary layer. *Experiments in Fluids*, 16:10–16, 1993.

[15] Y. Fu, P. Hall, and N. Blackenby. On the goertler instability in hypersonic flows: Sutherland law fluids and real gas effects. *Philisophical Transactions of Physical Science English*, 342:325–377, 1993.

[16] R. E. Spall and M. R. Malik. Goertler vortices in supersonic and hypersonic boundary layers. *Physics of Fluids A*, 1(11):1822–1835, 1989.

[17] A. Dufrene, M. Sharma, and J. M. Austin. Design and charachterization of a hypervelocity expansion tube facility. *Journal of Propulsion and Power*, 23(6):1185–1193, Nov 2007.

[18] M. Sharma. Further development and experimentation with the hypervelocity expansion tube. Master's thesis, University of Illinois, Urbana, IL, May 2007.

[19] W. Flaherty and J. M. Austin. Comparative surface heat transfer measurements in hypervelocity flow. In *48th AIAA Aerospace Sciences Meeting*. AIAA, Jan 2010.

[20] W. Flaherty and J. M. Austin. Comparative surface heat transfer measurements in hypervelocity flow. *Journal of Thermophysics and Heat Transfer*, 25(1):180–183, 2011.

[21] C. G. Miller. Comparison of thin-film resistance heat -transfer gages with thin-skin transient calorimeter gages in conventional hypersonic wind tunnels. NASA Technical Memorandum 83197, NASA, 1981.

[22] K. M. Chadwick. Stagnation heat transfer measurement techniques in hypersonic shock tunnel flows over spherical segments. AIAA-1997-2493, June 1997.

[23] C. T. Kidd. Coaxial surface thermocouples: Analytical and experimental considerations for aerothermal heat-flux measurement applications. *Proceedings of the ISA Aerospace Instrumentation Symposium*, 1990.

[24] C. T. Kidd, C. G. Nelson, and W. T. Scott. Extreaneous thermoelectrioc EMF effects resulting from press-fit installation of coaxial thermocouples in metal models. *Proceedings of the ISA Aerospace Instrumentation Symposium*, 1994.

[25] S. R. Sanderson. *Shock wave interaction in hypervelocity flow*. PhD thesis, California Institute of Technology, Pasadena, California, 1995.

[26] J. Davis. *High-Enthalpy Shock/Boundary-Layer Interaction on a Double Wedge*. PhD thesis, California Institute of Technology, Pasadena, California, 1999.

[27] A. Rasheed. *Passive Hypervelocity Boundary Layer Control Using an Ultrasonically Absorptive Surface*. PhD thesis, California Institute of Technology, Pasadena, California, 2001.

[28] M. J. Wright, J. Olejniczak, J. L. Brown, H. G. Hornung, and K. T. Edquist. Modeling of shock tunnel aeroheating data on the Mars Science Laboratory aeroshell. *Journal of Thermophysics and Heat Transfer*, 20(4):641–651, 2006.

[29] E. Marineau and H. Hornung. Modeling and calibration of fast-response coaxial heat flux gages. AIAA-2009-737, Jan 2009.

[30] I. I. Salvadaor, M. A. S. Minucci, P. G. P. Toro, A. C. Oliveira, and J. B. Channes Jr. Development of surface junction thermocouples for high enthalpy measurements. *American Institute of Physics Beamed Energy Propulsion: Fourth International Symposium*, 2006.

[31] S. Kuchi-ishi, S. Watanabe, K. Nakakita, T. Koyama, S. Ueda, and Katsuhiro. Comparative heat flux measurments between three hypersonic test facilities at NAL. AIAA-2003-4254, June 2003.

[32] M. S. Holden, T. P. Wadhams, M. G. Maclean, E. Mundy, and R. A. Parker. Experimental studies in LENS I and X to evaluate real gas effects on hypervelocity vehicle performace. AIAA-2007-204, January 2007.

[33] M. Maclean and M. S. Holden. Catalytic effects on heat transfer measurements for aerothermal studies with CO2. AIAA-2006-182, January 2006.

[34] P. A. Kinzie. *Thermocouple Temperature Measurement*. Wiley-Interscience, 1973.

[35] M. C. Croarkin, W. F. Guthrie, G. E. Burns, M. Kaeser, and G. F. Strouse. Temperature-electromotive force referance function and tables for the letter-designated thermocouple types based on the ITS-90. Monograph 175, National Institute of Standard Technologies, 1993.

[36] R. G. Adelgren. *Localized Flow Control with Energy Deposition*. PhD thesis, Rutgers University, New Brunswick, NJ, 2002.

[37] K. M. Kinnear and F. K. Lu. Design, calibration and testing and transient thin film heat transfer gauges. *AIAA Paper*, 1998.

[38] D. L. Schultz and T. V. Jones. Heat-transfer measurements in short-duration hypersonic facilities. Agardograph 165, AGARD, 1973.

[39] K. Asai, H. Kanda, C. T. Cunningham, R. Erausquin, and J. P. Sullivan. Surface pressure measurement in a crygenic wind tunnel by using luminescent coating. In *17th International Congress on Instrumentation in Aerospace Simulation Facilities*, Piscataway, NJ, 1997. Institute of Electrical and Electronics Engineers, Inc.

[40] H. Sakaue and J. P. Sullivan. Fast response time charachteristics of anodized aluminumn pressure senitive paints. In *38th Aerospace Sciences Meeting and Exhibit*, Reno, NV, January 2000. AIAA-2000-506.

[41] J. W. Gregory, K. Asai, M. Kameda, T. Liu, and J. P. Sullivan. A review of pressure-sensitive paint for high-speed and unsteady aerodynamics. *Proceedings of the Institutaion of Mechanical Engineers, Part G: Journal of Aerospace*, 222(2):249–290, 2008.

[42] L. Ciolkosz and E. Spina. An experimental study of Goertler vortices in compressible flow. *Experiments in Fluids*, 16:10–16, 1993.

[43] S. A. Berry, A. H. Auslender, A. D. Dilley, and J. F. Calleja. Hypersonic boundary-layer trip development for Hyper-X. *Journal of Spacecraft and Rockets*, 38(2):853–864, 2001.

[44] A. Paull and R. J. Stalker. Test flow disturbances in an expansion tube. *Journal of Fluid Mechanics*, 245:493–521, December 1992.

[45] P. A. Thompson. *Compressible-Fluid Dynamics*. McGraw-Hill Inc.

[46] J. A. Fay and F. R. Riddell. Theory of stagnation point heat transfer in dissociated air. *Journal of the Aeronautical Sciences*, 25(2):73–85, 1958.

[47] K. Sutton and A. R. Graves. A general stagnation-point convective-heating equation for arbitary gas mixtures. Technical report, NASA, 1971.

[48] F. De Filippis and M. Serpico. Air high-enthalpy stagnation point heat flux calculation. *Journal of Thermophysics*, 12(4):608–610, 1998.

[49] G. Simeonides. Gerneralized reference enthalpy formulations and simulation of viscous effects in hypersonic flows. *Shock Waves*, 8:161–172, 1998.

[50] E. R. Van Driest. Turbulent boundary layers in compressible fluids. *Journal of the Aeronautical Sciences*, 18:145–160, 1951.

[51] E. Marineau and H. Hornung. Heat flux calibration of T5 hypervelocity shock tunnel conical nozzle in air. AIAA-2009-4216, Jan 2009.

[52] R. N. Gupta. An analysis of the relaxation of laminar boundary layer on a flat plate after passage of an interface with application to expansion-tube flows. Technical report, NASA, 1973.

[53] E. Marineau, S J. Laurence, and H. Hornung. Apollo-shaped capsule boundary layer transition at high-enthalpy in T5. AIAA-2010-446, Jan 2010.

[54] W. Flaherty and J. M. Austin. Effect of concave wall geometry on heat transfer in hypersonic boundary layers. AIAA-2010-4986, January.

[55] W. Flaherty, J. Crafton, G. Elliott, and J. M. Austin. Application of fast pressure sensitive paint in hypervelocity flow. AIAA-2011-848, January.

[56] S. Mohammadian. Viscous interaction over concave and convex surfaces at hypersonic speeds. *Journal of Fluid Mechanics*, 55(1):163–175, 1972.

[57] H. K. Cheng, J. G. Hall, T. C. Golian, and A. Hertzberg. Boundary-layer displacement and leading-edge bluntness effects in high-temperature hypersonic flow. *Journal of the Aersospace Sciences*, 28(5):353–381, 1961.

[58] I. E. Beckwith. Heat transfer and skin friction by an integral method in the compressible laminar boundary layer with a streamwise pressure gradient. Technical Note 3005, NACA, 1953.

[59] M. Morduchow and R. G. Grape. Seperation, stability, and other properties of compressible laminar boundary layer with pressure gradient and heat transfer. Technical Note 3296, NACA, 1955.

[60] J. L. Stollery. Hypersonic viscous interaction on curved surfaces. *Journal of Fluid Mechanics*, 43(3):497–511, 1970.

[61] C. B. Cohen and E. Reshotko. The compressible boundary layer with heat transfer and arbitrary pressure gradient. Technical report, NASA, 1956.

[62] M. H. Bertram and W. V. Fuller. A simple method for determining heat transfer, skin friction, and boundary-layer thickness for hypersonic laminar boundary-layer flows in a pressure gradient. Memorandum, NASA, 1959.

[63] T. Li and H. T. Nagamatsu. Hypersonic viscous flow on a noninsulated flat plate. Memo 25, GALCIT, 1955.